ALMA MATER STUDIORUM · UNIVERSITY OF BOLOGNA

School of Science
Department of Physics and Astronomy
Master Degree in Physics

Overcoming paraffin embedding constraints in the analysis of FFPE tissue samples with μ-EDXRF and polarized XRF

Supervisor:
Prof. Nico Lanconelli

Co-supervisor:
Prof. Alda Sofia Pessanha de Sousa Moreno

Submitted by:
Sara Pandolfi

Academic Year 2022/2023

Acknoledgement

This master thesis has been carried on in collaboration with the LIBphys Lab of the NOVA University of Science and Technology of Lisbon, thank to the opportunity gave me by the Erasmus+ program.

I would like to express my gratitude to my advisor, Professor Sofia Pessanha, and to her colleagues Professor Jorge Machado and Professor Luísa Carvalho for having proposed me this international project and for having kindly welcomed me. I would also thank my lab colleagues Gonçalo, João and Rúben for sharing with me this international experience.

Finally, I would like to thank whom provided me the tissue datasets used in this study, *Instituto Português de Oncologia de Lisboa Francisco Gentil* and *NOVA Medical School*, in particular Professor Ana Félix and Doctor Fernanda Silva.

Abstract

Every time an intervention is performed, the total (biopsy) or a portion (surgery) of normal and tumor tissue is retrieved and processed as Formalin Fixed Paraffin Embedded (FFPE) blocks for the diagnosis and after they are stored for safekeeping. These FFPE blocks contain precious information regarding the elemental composition of normal/tumor tissue that is not harvested because there is no suitable analytical tool for elemental analysis of these samples. In what regards EDXRF, paraffin embedding process alters the sample's matrix permanently, hindering the application of common quantitative approaches based of Certified Reference Materials (CRMs). In this work a total of 19 sets of mirrored tissue samples collected from IPO (Instituto Português de Oncologia de Lisboa Francisco Gentil) and from NMS (NOVA Medical School), were analyzed, processed as pellets or after FFPE, in order to develop calibration curves and parametrize the influence of paraffin in the intensity of elemental peaks in the EDXRF spectrum. Measurements were performed using three different EDXRF systems: μ-EDXRF spectrometer Tornado from Bruker using two different filter configurations, a Benchtop spectrometer with triaxial geometry and a secondary target of Mo, and a portable spectrometer with triaxial geometry and changeable secondary target (Y and Ge). By using its two different secondary targets, the portable system provided insights of the thickness of the tissues. However, it was not employed for building calibration curves, due to the incompatibility of its beam size with most of the dimensions, in particular the width, of the tissues inside the FFPE blocks.

Calibration curves for S, Ca, Ti, Fe, Cu and Zn were obtained from Tornado, while for Ca, Fe, Cu, Zn and Br were obtained from the Benchtop triaxial system. The curves were build after the normalization of the characteristic elemental intensities for the tube excitation source Compton-to-Rayleigh ratio. Per each element one set of samples was kept out from the building of the curve and was used for validation, by comparison of the intensity obtained in the FFPE tissue block and as pellet (true value). Results show that using this procedure the obtained intensities present a bias towards the true value lower than 9% for most of the elements, with the exception of Br (35%). Eventually the quantification of the intensity peaks was performed for pellets and FFPE blocks and compared. For most of the samples, among the measurements collected from the Benchtop and Tornado systems, results show that using this procedure the obtained concentration for S, Ca, Fe, Cu and Zn present a discrepancy towards the true value lower than 30%. On the other hand, precision of the method is too low, indicating the need to increase sample size and reduce the uncertainty of the method.

Contents

Introduction

Trace elements play an important role in biological processes and the understanding of the mechanisms of their assimilation may be indicative of the genesis or progression of diseases. Despite their importance, the elemental composition of human tissues is prone to high variability. Only a global and statistically significant knowledge of the elemental content of normal human tissues and its comparison with, for instance, tumoral ones, might bring to the discovery of elemental biomarkers for cancer. This thesis intends to overcome this obstacle by taking advantage of the vast repository of human tumor tissues processed as Formalin Fixed Paraffin Embedded (FFPE) blocks the diagnosis and then stored for safekeeping in hospitals, using Energy Dispersive X Ray Fluorescence, a non-destructive analytical technique. FFPE blocks contain precious information regarding the elemental composition of the tissue but there is no suitable analytical tool for elemental analysis of these samples. Concerning EDXRF, paraffin embedding process alters the sample's matrix permanently, hindering the application of common quantitative approaches based of Certified Reference Materials (CRMs). The External Standard quantification approach uses CRMs to determine the concentration of an unknown specimen by comparing its fluorescence intensity with the one of an accurately known specimen, if they have similar matrix. CRMs and tissues lyophilized, powdered and pressed into pellets have a comparable mean-Z values, and consequently also their matrix, allowing the quantification of the elements stored in this form. For this study three sets of paired pellet-FFPE blocks tissues for a total of 19 samples have been used to parametrize the effects of paraffin embedding on the resulting elemental intensity peaks.

Chapter 1

Theoretical Concepts

This section provides a review of the main concepts necessary to carry this work. Firstly, a brief medical introduction shows how the study of trace elements in the understanding of cancer can be important and how the human tissues need to be treated for long term storage. Secondly, the physics of the used XRF instruments is reviewed in order to understand how the spectra are acquired and what are they showing. Finally, an overview of the quantification of the XRF spectra is reported to help finding an interpretation of the obtained results.

1.1 Medical background

1.1.1 Relevance of Trace Elements in Medicine

Cancer, characterized by uncontrolled cell growth and its spread to other organs, remains a leading global cause of death, accounting for nearly 10 million deaths in 2020 as reported by WHO [1]. In light of this, numerous epidemiological investigations have been conducted to identify potential cancer risk factors. Notably, the composition of the average human body consists of four main elements (H, O, C, and N) comprising about 99% of its weight. The remaining portion comprises essential elements (Na, K, Mg, Ca, Cl, P, S) and trace elements (Mn, Fe, Cu, Zn, Se). The physiochemical properties of these trace metals significantly influence their uptake, intracellular distribution, and binding to metal compounds within biological systems. Such interactions can interfere with cellular redox regulation, leading to the production of oxidative stress, causing oxidative DNA damage, or triggering signaling cascades that might stimulate malignant growth [2].

1.1.2 Handling and Preparing Human Tissue Samples

Every time an intervention is performed, the total (biopsy) or a portion (surgery) of normal and tumor tissue is retrieved and processed as Formalin Fixed Paraffin Embedded (FFPE) blocks for the diagnosis and after they are stored for safekeeping. However, tissue samples can also be lyophilized by being frozen-dried, powdered and then compacted into pellets. For histopathological investigations the fixation and embedding procedure is the most suitable, since the lyophilization process powders the tissue, hindering its structure study. Therefore, the sample is embedded in paraffin to provide the necessary conditions for routine hospital analysis.

FFPE are formed by immersing the tissue into formalin, an aqueous solution of formaldehyde (CH_2O) used for fixing a tissue to preserve proteins and vital structures within it. After

the formalin fixation, the tissue must undergo a progressive dehydration by immersion in alcohol, since the paraffin is not soluble in water. Then, it is incubated in xylene to clear the alcohol before embedding in a paraffin wax heated to 60 ºC. Paraffin is a hydrocarbon compound (C_nH_{2n+2}) solid at room temperature and begins to melt above, approximately, 37 °C. Finally, for histopathological purposes, using a microtome, the tissue can be cut into thin slices of 1-50 μm thicknesses and then stored at room temperature [3].

For what concerns lyophilization, the biological tissue is freeze dried, which involves the removal of solvents (mostly water) from the material through sublimation. The solid frozen material is converted directly to the gaseous phase without passing through the liquid phase [4]. Then the freeze dried sample is reduced in an homogeneous powder and pressed into a pellet that can be used for further studies.

1.2 Physics of XRF

1.2.1 Properties of X-Rays

Electromagnetic waves permeate the universe. They arise from a changing magnetic field that induces a changing electric field (and vice-versa). The spectrum of waves ranges from short and highly energetic γ-rays to long radio waves.

X-rays constitute a fraction of the electromagnetic spectrum, overlapping γ-ray and approaching ultraviolet radiation, as depicted in Figure 1.1. With wavelengths falling within the range of 5×10^{-12} to 10^{-10} m, they correspond to energies spanning from 0.125 to 125 keV [6]. The wavelength of X-rays is inversely proportional to their energy, as given by the equation:

$$E = h \cdot \frac{c}{\lambda} \tag{1.1}$$

where E denotes the energy (in keV), h represents Planck's constant (4.14×10^{-15} eVs), c stands for the speed of light (3.00×10^{8} m/s), and λ indicates the wavelength (in nm).

X-rays are produced through the deceleration of high-energy electrons and electron transitions within the inner orbitals of atoms. They travel in straight lines, remain invisible, and are imperceptible to any other human sense. Upon striking matter, X-rays can be transmitted, reflected, diffracted, scattered, or undergo photoelectric absorption.

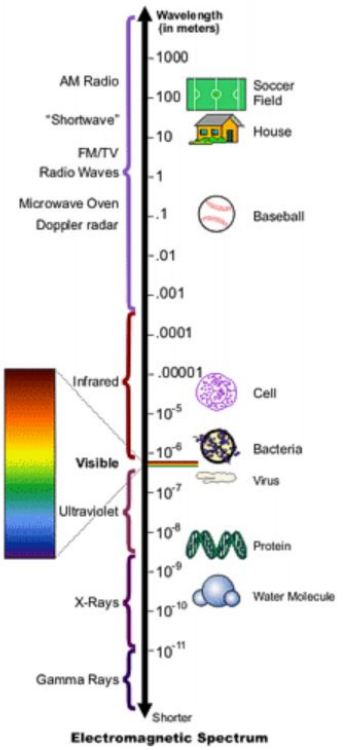

Figure 1.1: Representation of the electromagnetic spectrum [5]

X-Ray Fluorescence (XRF) Spectroscopy uses only a small portion of the X-ray spectrum and it is based on the emission of continuous radiation, which takes place when high-energy charged particles cross the coulomb field of an atom nucleus, and characteristic radiation, emitted when orbital electrons of atoms in a target transit between allowed energy states.

1.2.2 Interaction of X-Ray with matter

The short wavelengths of X-ray radiation and the high penetration into material provide different possibilities for the examination of material. Possible interactions of X-ray with matter are

absorption, scattering or diffraction, refraction, emission and transmission.

Absorption

When an X-ray beam interacts with a material characterized by an atomic number Z, it undergoes attenuation. This interaction is described by the mass absorption coefficient, μ, which is the sum of the absorption coefficient τ and the scattering coefficient σ, both measured in cm^2/g.

The process of attenuation can be explained using Lambert-Beer's law, where the mass attenuation coefficient μ, the material density ρ, and the thickness of the material t play crucial roles in the absorption of the incident radiation. The law states that the intensity of the radiation, denoted by I(λ_0), after passing through matter can be expressed as:

$$I(\lambda_0) = I_0(\lambda_0)e^{-\mu\cdot\rho\cdot t} \tag{1.2}$$

where I(λ_0) is the initial intensity of the radiation, μ (measured in cm^2/g) represents the mass attenuation coefficient as a function of energy (or wavelength) of the radiation, ρ (in g/cm) is the density of the absorbing material, and t (in cm) is the thickness of the absorbing layer. The mass attenuation coefficient in equation 1.2, depends on the energy of the radiation, therefore it depends on the radiation wavelength, λ_0. When the material consists of distinct elements, the overall mass attenuation coefficient can be calculated by summing up the contributions from each element's mass attenuation coefficient μ_i, multiplied by their respective mass fraction w_i:

$$\mu_{compound} = \sum_i w_i\mu_i \tag{1.3}$$

where w_i denotes the mass fraction of element i and μ_i represents the mass absorption coefficient of that element [7].

Scattering

Scattering refers to the interaction of an X-ray photon with electrons and can be described using classical electromagnetic theory or the particle model for the X-ray photon.

In the case of elastic scattering, also known as coherent scattering or Rayleigh scattering, there is no energy loss. As a result, the coherently scattered radiation retains the same wavelength as the incident beam, with a definite phase relationship between them. During this process, the atom remains neither ionized nor excited (Figure 1.2 left).

The Rayleigh formula describes this phenomenon for randomly distributed directions of the electromagnetic field of the X-rays as follows:

$$I_{RScat} = I_0\frac{1}{r^2}\left(\frac{e^2}{m_0}\right)^2(1+\cos^2\phi_2) \tag{1.4}$$

where I_{RScat} represents the scattered intensity, I_0 is the primary intensity, r denotes the distance to the observation point, e is the charge of an electron, m_0 is the mass of an electron, and ϕ_2 is the scattering angle. Scattering angles close to 90° lead the scattered intensity toward its minimum, while scattering angles ϕ_2 close to 0° or 180° result in a maximum scattered intensity.

Compton scattering, on the other hand, is described by the corpuscular nature of the X-ray photon, and it conserves both energy and momentum. This interaction occurs with a weakly bound electron considered to be at rest. During the collision, the electron recoils, removing

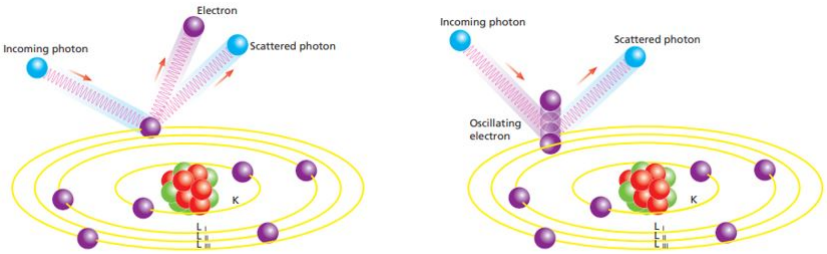

Figure 1.2: Representation of the Rayleigh (left) and Compton (right) scattering. Adapted from [8]

a small portion of the photon's energy, and gets deflected, resulting in an increase in wavelength (Figure 1.2 right). As a consequence, Compton scattering is also known as incoherent or inelastic scattering. The wavelength of the scattered radiation λ_{Scat} is described by:

$$\lambda_{Scat} = \lambda_0 + \lambda_c \cdot (1 - \cos\phi_2) \tag{1.5}$$

where λ_0 denotes the wavelength of the incident photon, $\lambda_c = \frac{h}{mc}$ represents the Compton wavelength, and m is the mass of the scattering particle (electron in this case) [7].

Elastic and Inelastic Cross Sections

The differential cross sections, defined as the ratio of the number of photons scattered in a particular direction to the number of incident photons, for the Compton and Rayleigh scattering on bound electrons can be derived from the inelastic Klein-Nishina (Eq. 1.6) or elastic Thompson (Eq. 1.7) scattering on free electrons cross sections respectively, which are energy (E) and angle (θ) dependent:

$$\frac{d\sigma_{KN}}{d\Omega} = \frac{r_0^2}{2}\left[\frac{1}{[1+\alpha(1-\cos\theta)]^2} \cdot \left[1 + \cos^2\theta + \frac{\alpha^2(1-\cos\theta)^2}{1+\alpha(1-\cos\theta)}\right]\right] \tag{1.6}$$

$$\frac{\sigma_{Th}}{d\Omega} = \frac{r_0^2}{2} \cdot [1 + \cos^2\theta] \tag{1.7}$$

They are measured in $cm^2 str^{-1} el^{-1}$, where $\alpha = \frac{E_0}{511}$ (keV) and r_0 =2.818×10^3 (cm), *str* indicates steradiants, and *el* is electron. From these the Compton (Eq. 1.8) and Rayleigh (Eq. 1.9) are obtained compiling the two functions, $F(q, Z)$ and $S(q, Z)$, constituting the atomic form factor and the incoherent scattering function, respectively [9]:

$$\frac{d\sigma_{Compton}(E,\theta)}{d\Omega} = \frac{d\sigma_{KN}(E,\theta)}{d\Omega} \cdot S(q, Z) \tag{1.8}$$

$$\frac{d\sigma_{Rayleigh}}{d\Omega} = \frac{d\sigma_{Th}(E)}{d\Omega} \cdot F^2(q, Z) \tag{1.9}$$

which are measured in $cm^2 str^{-1} atom^{-1}$. The functions $F(q, Z)$ and $S(q, Z)$ are compiled by Hubbel et al. [9] in the form of tabulated values in dependence on q, the momentum transfer from the X-ray photon interacting with a particular electron, in a well defined bound state, in the atom, and Z, the average atomic number of the target.

Diffraction

Diffraction is a phenomenon that results from the combination of coherent scattering and interference, where one wave superimposes upon another. When a beam of monochromatic X-rays strikes a crystal lattice, it produces a diffracted beam with specific directions. This reinforcement condition for reflection, known as Bragg's law, occurs only when the difference in the path-lengths of the two interfering waves equals a whole number of wavelengths, represented by λ:

$$n\lambda = 2d \cdot sin\phi_1 \tag{1.10}$$

where n is the order of reflection, d is the interplanar spacing and ϕ_1 is the scatter angle.

Refraction

When X-rays pass through areas with different optical densities, they are refracted. X-rays refraction is primarily influenced by the density of the material. Materials with higher density exhibit less refraction. Refraction plays a significant role and can be utilized for beam shaping in XRF instruments [7]. The refractive index n can be expressed as follows:

$$n = 1 - \delta + i\beta \tag{1.11}$$

Here, δ represents a potential deviation, and β stands for the absorption coefficient.

Polarization by reflection

Polarization is a property of transverse waves which specifies the geometrical orientation of its oscillations. Electromagnetic waves are transverse waves in which the oscillating electric and magnetic components are perpendicular to each other and the direction of their oscillation is perpendicular to the direction of propagation of the wave. Fresnel equations state that the reflectivity of the parallel and perpendicular component of the transverse wave are:

$$\begin{aligned} R_p &= \left|\frac{n_1\cos\theta_t - n_2\cos\theta_i}{n_1\cos\theta_t + n_2\cos\theta_i}\right|^2,\ \gamma \parallel \Pi_{in} \\ R_s &= \left|\frac{n_i\cos\theta_i - n_r\cos\theta_t}{n_i\cos\theta_i + n_r\cos\theta_t}\right|^2,\ \gamma \perp \Pi_{in} \end{aligned} \tag{1.12}$$

where R_s is the reflectivity of the photons with electric field vector perpendicular to the plane of incidence Π_{in}, R_p is the reflectivity of the parallel polarized photons, θ_i is the incident and θ_t the transmitted photon angle s and the refracting index of the media are n_1 and n_2.

Recalling Snell's law for refraction:

$$\frac{\sin\theta_i}{\sin\theta_t} = \frac{n_2}{n_1} \tag{1.13}$$

using Brewer's angle $\left(\tan\theta_{1B} = \frac{n_2}{n_1}\right)$, along with the condition $\theta_{iB} + \theta_r = \frac{\pi}{2}$, the incident radiation can be polarized:

$$\begin{aligned} \sin\theta_t = \tfrac{n_1}{n_2}\sin\theta_{iB} = \tfrac{n_1}{n_2}\cos\theta_{iB}\tan\theta_{iB} = \cos\theta_{iB} \\ n_1\cos\theta_t - n_2\cos\theta_{iB} = n_1\sin\theta_{iB} - n_2\sin\theta_t = 0 \end{aligned} \tag{1.14}$$

resulting in $R_p = 0$, transmitting completely the parallel component $T_p = 1 - R_p$, as shown in Figure 1.3.

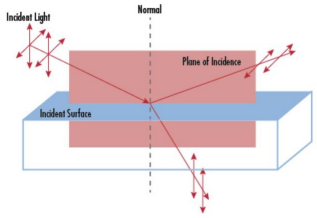

Figure 1.3: Representation of polarization by reflection, adapted from [10].

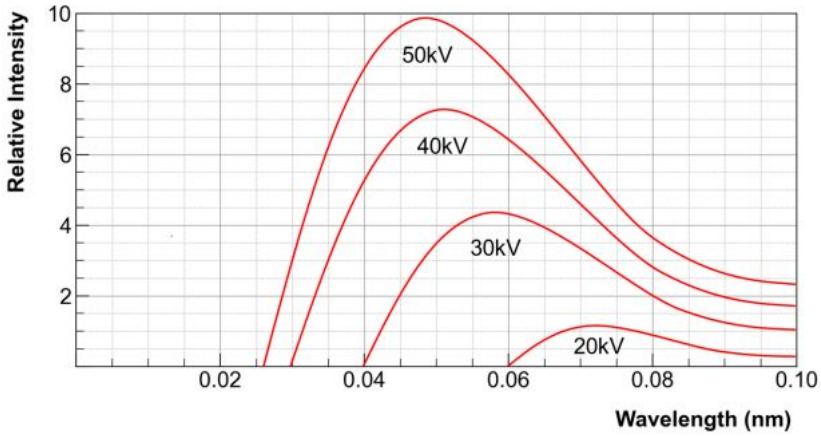

Figure 1.4: Plot of the relative bremsstrahlung Radiation as a function of energy for different accelerating voltages.

For what concerns XRF, it is possible to add a secondary target to reflect the X-rays and select the Brewster angle in order to filter out the bremsstrahlung radiation. Recalling that the index of refraction of every material for radiation with energies greater than 1 keV is close to unity, the resulting Brewster angle for X-rays is approximately $\theta_{iB} = 45°$. As a consequence, the reflection angle is also of 45° [11].

Emission of Continuous Radiation

According to classical electromagnetic theory, when high-energy charged particles pass through the Coulomb field of an atom's nucleus, they experience deceleration, leading to the emission of a broad wavelength band of radiation known as Bremsstrahlung Radiation (BR) (Figure 1.4)[6]. The continuous X-ray spectrum produced by electrons in an X-ray tube is characterized by a short-wavelength limit, denoted as λ_{min}, which corresponds to the maximum energy of the exciting electrons:

$$\lambda_{min} = \frac{hc}{eV_0} \tag{1.15}$$

In this equation, h represents Planck's constant, c is the velocity of light, e is the electron charge, and V_0 is the potential difference applied to the tube. This relationship between the short-wavelength limit and the applied potential is known as the Duane–Hunt law.

The probability of bremsstrahlung radiation occurrence is influenced by the target and the incident particle, and it can be expressed as follows:

$$P_{Brems} \propto \frac{q^2 Z^2 T^2}{M_0^2} \tag{1.16}$$

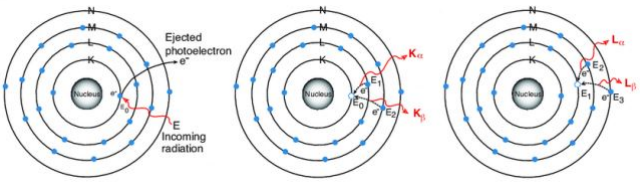

Figure 1.5: Representation of the emission of characteristic radiation following the ejection of an electron from the K shell and filled by an electron coming from the L shell, known as Kα.

where q represents the particle charge in units of the electron charge e, Z is the atomic number of the target, T is the kinetic energy of the incident particle, and M_0 is the rest mass of the particle.

The intensity of continuous X-ray generated by electrons is significantly higher than the one generated by heavier particles due to their larger masses. The maximum intensity of the bremsstrahlung radiation distribution, denoted as I_{max}, occurs at a wavelength between 1.5 to 2 times greater than λ_{min}. Additionally, in Figure 1.4, it is evident that the intensity distribution of the continuum shifts towards shorter wavelengths as the accelerating potential increases [6].

Emission of Characteristic Radiation

When orbital electrons of atoms in a target transit between allowed energy states, they emit radiation that is characteristic of that transition, known as characteristic X-ray [6]. This phenomenon occurs when a high-energy particle interacts with a bound atomic electron, causing it to be ejected from its atomic position and creating a vacancy if the energy of the first particle (E) exceeds the binding energy of the electron (ϕ).

When the high-energy particle is a photon, the interaction is commonly referred to as the Photoelectric Effect (PE), where the kinetic energy of the electron becomes equal to $E - \phi$ [6, 7].

The atom remains in an unstable state as long as the vacancy in the shell exists. However, the transfer of an electron from one of the outer orbitals to fill the vacancy restores its stability, as shown in Figure 1.5. For example, if an electron is ejected from the K shell, the atom becomes ionized and the ion is left in a high-energy state. The excess energy the ion has over the fundamental state is equal to the energy required to remove the K electron to a state of rest outside the atom. If this electron vacancy is filled by an electron coming from an L shell, the transition is followed by the emission of an X-ray line known as the Kα line. This process leaves a vacancy in the L shell. On the other hand, if the atom contains sufficient electrons, the K shell vacancy might be filled by an electron from the M shell (Kβ line). The remaining L or M state ions may also emit radiation until the vacancy is at the highest level.

Only a limited number of transitions is allowed by the theory of X-ray, and they are driven by selection rules that can be expressed as [6, 7]:

$$\Delta l = \pm 1, \quad \Delta j = 0 \text{ or } \Delta j = \pm 1 \tag{1.17}$$

where the transition $j \rightarrow 0$ is forbidden.

Moseley established the relationship between the wavelength of an X-ray characteristic line and the atomic number Z of the corresponding element, allowing its identification. Moseley's law is written as [12]:

$$\frac{1}{\lambda} = k(Z - \sigma)^2 \tag{1.18}$$

where k is a constant that takes on different values for each spectral series, and σ is a shielding constant for the repulsion correction due to other electrons in the atom.

The radiative transition occurs only with the emission of characteristic radiation, and the probability of this radiative transition is called the fluorescence yield w, which depends on the energy. The definition of the fluorescence yield becomes more complicated for higher atomic numbers since there are more than one subshell for shells above the K shell, and Coster-Kronig (CK) transitions might occur [13]. If there are no CK transitions, the fluorescence yield of the i^{th} sub-shell of a shell is given as:

$$w_i^X = \frac{I_i^X}{n_i^X} \tag{1.19}$$

where I_i^X is the total number of characteristic K X-ray photons emitted from a sample, and n_i^X is the number of primary X shell vacancies, where X is the principal quantum number (X = K, L, M, ...) [6].

Auger Effect

As mentioned above, removing one electron from an inner shell of an atom results in an excess of energy in the atom. However, this excess energy does not necessarily lead to the emission of X-ray photons [6]. Instead, the Auger effect can occur when photoelectrons are emitted from the atom instead of X-ray photons. Consequently, the atom is left in a doubly-ionized state with two missing electrons, and the electron that is emitted carries away an energy of $E_{Auger} = E_{excess} - E_{binding}$.

The probability of the Auger effect increases when the difference between the corresponding energy states decreases [6, 7]. Furthermore, Coster-Kronig (CK) transitions are specific cases of the Auger effect and involve nonradiative transitions between the subshells of an atomic shell.

1.3 X-Ray Fluorescence Spectroscopy

X-ray fluorescence refers to the emission of characteristic X-rays from a material that has been stimulated by incoming X-ray radiation. The core components of XRF spectrometers comprise a radiation source that irradiates the sample and a detector responsible for measuring the emitted radiation. There are two possible spectrometers setups:

- Energy Dispersive XRF (**EDXRF**) employs a detector capable of discerning the energies of photons, as illustrated in Figure 1.6a. It enables simultaneous measurement of all elements and utilizes a specialized X-ray detector to provide voltage pulse distributions proportional to the energy of emitted photons. In EDXRF systems different types of X-ray sources can be used, such as synchrotron radiation sources, radioactive sources and X-ray tubes. Also different geometry setups can be adopted. Among these, X-ray tube-based systems were utilized in this study due to their suitability for laboratory applications, particularly in the analysis of biological tissues. EDXRF presents several advantages, including affordability and rapid measurement times. However, the energy resolution due to broad overlapping peaks is a disadvantage. The EDXRF setup is also not very suitable for light elements. Total Reflection X-ray Fluorescence (TXRF) and micro X-ray Fluorescence (μXRF) are two variations that come from EDXRF. While in TXRF the angle between the X-ray tube and the sample is almost identical to the total reflection angle of X-ray in a reflector Si wafer, allowing that only the photons emitted by

fluorescence phenomena are detected, in μXRF the X-ray are focused to a much smaller area, improving the spatial resolution.

- Wavelength Dispersive XRF (**WDXRF**) uses a crystal to filter the incoming radiation based on wavelength, as shown in the Figure 1.6b. In the crystal, the X-ray are scattered from different layers of atoms, which means that some beams travel a longer optical path. As an advantage, it presents greater accuracy than the EDXRF setup. It is well suited for lighter or heavier elements. However, it has some disadvantages, such as longer measurement times and significantly higher cost of the spectrometer.

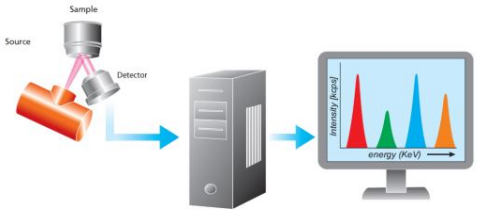

(a) Illustration of a typical EDXRF Setup, from [8].

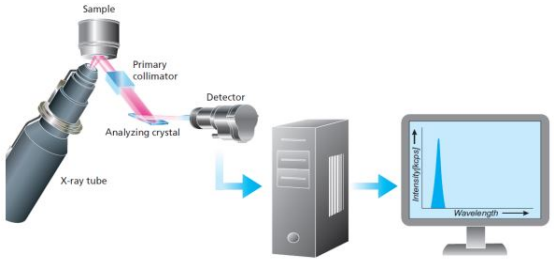

(b) Illustration of a typical WDXRF Setup, from [8].

1.3.1 X-Ray Spectra

The X-ray spectrum obtained from EDXRF shows characteristic Rayleigh and Compton peaks of the source material. In Rayleigh scattering, photons emitted by the X-ray source strike the sample's substrate, changing their trajectory without losing energy, while in Compton scattering, photons lose energy upon striking the sample. This results in an adjacent peak on the left side (lower energy) of the characteristic anode peak associated with Rayleigh scattering.

The shape of the spectrum depends on the geometry of the acquisition system:

- **Direct X-Ray tube excitation** The X-ray spectrum consists of a well-defined continuum and sharp characteristic lines, as can be seen in Figure 1.7a. The bremsstrahlung radiation is described by Kramers's formula [6]:

$$\begin{aligned} I(\nu)d\nu &= \frac{16\pi^2 AZ^2e^5}{3\sqrt{3}m_0V_0c^3}, \quad \nu < \nu_0 \\ I(\nu)d\nu &= 0, \qquad\qquad\quad \nu > \nu_0 \end{aligned} \tag{1.20}$$

  where $I(\nu)d\nu$ represents the intensity of the continuous X-ray within a frequency range $(\nu, \nu + d\nu)$, Z is the atomic number of the target material, ν_0 is the cutoff frequency $(\frac{c}{\lambda_{min}})$ above which the intensity is zero, and A is the atomic mass of the target material.

  The spectrum background results from Compton and Rayleigh interactions of each photon in this bremsstrahlung radiation. The absorption of photons in the detector and sample causes a decrease in the continuous radiation at low energies. Due to various nuclear processes contributing to this radiation, it is challenging to derive a real physical model.

- **Triaxial geometry excitation** Bremsstrahlung can be removed when the X-ray radiation interacts with a secondary target, scattering the beam at an angle of 90°, as can be noticed in the Figure 1.7b. This setup exploits the polarization of the radiation in the secondary

target and in the sample. The sample is excited by a practically monochromatic energy and the resulting spectrum is composed of the characteristic peaks of the sample and the Rayleigh and Compton Kα and Kβ peaks of the secondary target [14].

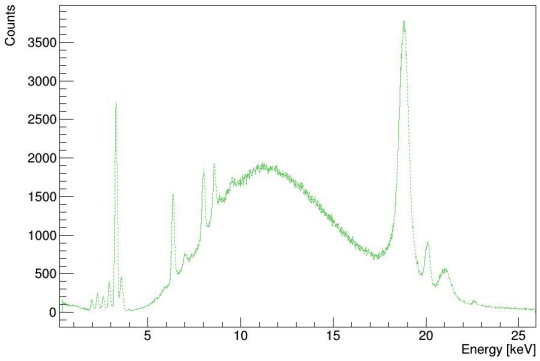

(a) Spectrum acquired with direct x-Ray tube of Rh excitation, showing at 20.216 keV the Rayleigh peak of Rh Kα and at its left the associated Compton Kα.

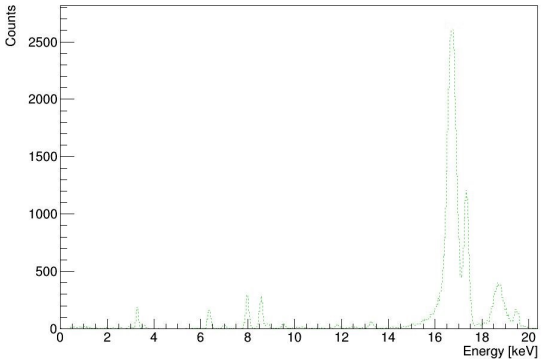

(b) Spectrum acquired with a triaxial geometry and tube of Mo, showing at 17.480 keV the Rayleigh peak of Mo Kα and at its left the associated Compton Kα.

Figure 1.7: Example of spectra of the Certified Reference Material Bovine Liver acquired in a direct tube excitation and with a triaxial system.

1.3.2 Silicon Drift Detector

The Silicon Drift Detector (SDD) is the most used detector for Energy-Dispersive spectroscopy equipment as it features excellent energy resolution at high count rates. The radiation reaching the detector Si bulk material results in the formation of more electron-hole pairs whose number, n, depends on the fixed energy in the detector, E_{EHP}, and the energy with which the radiation reaches the detector, E_x, resulting in $n = \frac{E_x}{E_{EHP}}$.

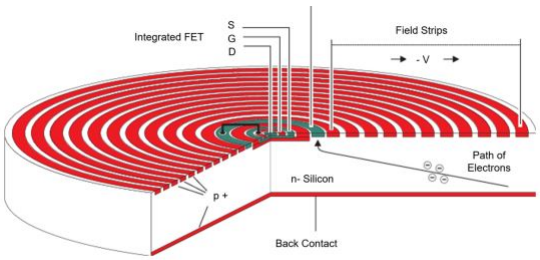

Figure 1.8: Section of a SDD of Thermofisher [15]

Figure 1.8 provides a schematic representation of this detector configuration, a collection of circular electrodes on its rear surface. These electrodes are designed with a field gradient to capture the charge generated by incoming X-rays. Subsequently, the liberated electrons undergo pre-amplification using a Transistor Field Effect (FET) mechanism, which transforms the electric charge into a voltage output. Finally, the detector chip is affixed to a thermoelectric cooling system, ensuring efficient device cooling as detailed in [15]. The main features that chatacterize a detector are its energy resolution, sensitivity, efficiency and thickness of the window. The energy resolution of a detector is the ability to distinguish two photons with very

close energies while the sensitivity corresponds to the capacity to produce pulses for a given energy range. The efficiency of a detector is determined by the number of photons detected in relation to the number of photons emitted by the X-ray source and the sample.

The characteristic radiation of an X-ray line follows a Lorentz distribution. However, the peaks observed in the spectrum from a semiconductor detector are the convolution of this distribution with the response function of the detector itself. The tails appearing on the left side of the peaks are due to incomplete charge collection resulting from detector imperfections (dead layer and areas of low electric field). Nevertheless, the accuracy of the recorded spectrum can be affected by amplitude and energy noise. Amplitude noise results from the statistical nature of the counting process, as photons arriving at the detector occur over random events during a finite period. This noise can be reduced by acquiring the spectrum for a longer period or by increasing the intensity of the primary beam. The energy noise results from the electronic conversion process in the detector. Occasionally, photons of energy E which correspond to a pulse height in channel i are associated with higher/lower pulses which causes them to be stored in the channels above/below [7].

Detection Limit

The Detection Limit (DL) of a certain system is determined by the minimum concentration of the studied element that could be detected by the system and it is given by [16]:

$$DL = 3\frac{C_i\sqrt{N_b}}{N_p} \tag{1.21}$$

indicating with C_i the concentration of element i, N_p corresponds to the count rate of the corresponding fluorescence peak and N_b corresponds to the background count rate.

1.3.3 Spectra artifacts

When X-ray photons interact with a detector, several artifacts can arise:

- **Pile-up peaks** occur when two photons arrive at the detector simultaneously, and the electronic circuitry of the preamplifier is unable to distinguish their individual energies. The detector registers a single event with an energy equivalent to the sum of the energies of the detected photons.
- **Escape peaks** result from the interaction of photons emitted by the sample with the semiconductor material at the ends of the detector. This interaction excites atoms within the semiconductor, leading to the emission of characteristic radiation from the semiconductor material (e.g., silicon, germanium, iodine). These emitted photons escape the detector. As a result, the detected photons lose energy and are registered with lower energies than they had upon arrival at the detector. The energy of the escape peak is the difference between the energy of the detected photon and the energy of the emitted semiconductor photon [8].

1.4 Quantification in XRF Analysis

In X-ray fluorescence (XRF) analysis, the process of quantifying elements involves converting measured fluorescent intensities into analyte concentrations. However, this task is far from

straightforward. The measured intensities are influenced not only by the concentration of the analytes but also by factors such as accompanying elements (matrix), sample type (solid, liquid, or powder), sample preparation methods, sample shape and thickness, and measurement conditions [17]. There are two main categories of methods used to address and correct the effects of matrix presence in a given sample: matrix correction methods and compensation methods.

- **Matrix correction methods** do not necessitate specific sample preparation and all the interactions can be described by physical models. There are two main methods:

    1. **Fundamental Parameter Method**: this method employs iterative processes to ascertain the composition of a sample. Initially assuming a composition for the sample, theoretical intensities are compared with experimental intensities. The composition is then adjusted iteratively until the theoretical and experimental spectra align. However, this method may not be suitable for human tissues due to the presence of elements, such as H, C, N, and O, that are not easily detected in XRF spectra but significantly influence trace element detection.
    2. **Influenced Coefficient Algorithms**: this method involves deriving numerical coefficients that mathematically correct the impact of matrix effects on detected radiation intensity. These coefficients are obtained through regression-based mathematical formulas. The calculation of these coefficients involves solving systems of equations, with the number of equations being equal to or greater than the number of coefficients to be determined. Hence, the number of sample standards must exceed the number of elements to be quantified.

- **Compensation methods** have some drawbacks compared to matrix correction methods (e.g., sample preparation requirement, limited quantification of elements), but among these there is the most suitable one for the quantification of human tissues. There are three compensation methods:

    1. **Internal Standard Method**: it consists of introducing a known quantity of an element that is not naturally present in the sample but shares similar fluorescence properties. The peak intensity corresponding to that element is then used as a standard for quantifying the other components in the sample. This method is appropriate for thin samples 1.4.2, as while the sample thickness increases, linearity is lost, and matrix elements must be considered.
    2. **External Standard Method**: as thickness increases, matrix elements must be considered. This method mitigates the issue by quantifying components in an unknown sample by comparing them to Certified Reference Materials (CRMs) with similar compositions. This calibration curve method allows for quantification in different matrices, such as human tissues. It is especially advantageous for quantifying elements present in low concentrations. It is required that the matrix remains constant during the comparison in this procedure.
    3. **Standard Addition Method**: this approach involves introducing the element of interest into the sample at predefined concentrations and assessing the effects of this addition. However, this method is less suitable for elements in low concentrations due to sample preparation requirements and difficulties in obtaining known concentrations.

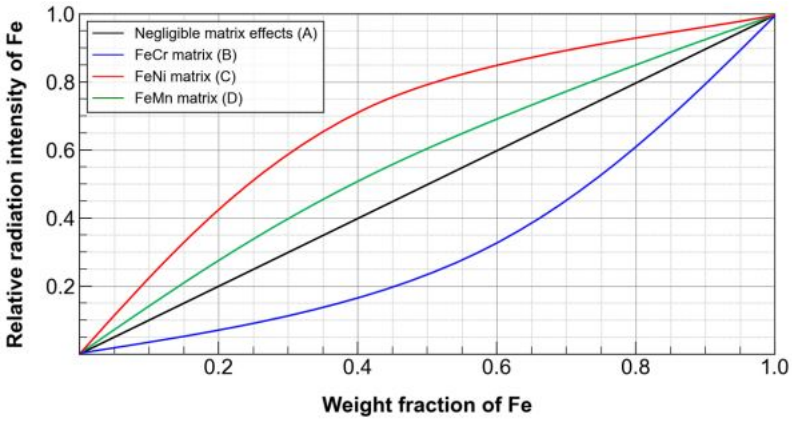

Figure 1.9: Variation of radiation intensity of Fe with its weight fraction and chemical compound [17].

1.4.1 Matrix Effects

The peak intensity of a given element in the spectrum is proportional to its concentration in the sample. The intensity of a peak corresponding to a specific element in a spectrum is directly proportional to the concentration of that element within the sample. However, as most samples are not infinitely thin (1.4.2), the quantification process is subject to matrix effects that arise from two distinct phenomena: the attenuation of characteristic X-ray emitted by a particular element and the enhancement of characteristic X-ray from other elements present in the sample, apart from the element under analysis. When the elements of the sample absorb the primary radiation, it is called primary absorption, whereas when the characteristic radiation is absorbed, it is called secondary absorption. The enhancement effect comes into play when the emission of characteristic radiation with higher energy than the absorption energy of the element under examination is observed. This signifies that the element was excited and emitted radiation beyond what originated from the primary X-ray source. In Figure 1.9, these effects are illustrated: FeCr, FeMn, and FeNi binaries are used as examples where Fe has the same concentration in all compounds, but the matrix is different, providing different results. Curve *A* shows a linear relationship between the radiation intensity and the weight fraction of Fe because the matrix effects are negligible. For FeCr, since the characteristic energy of Fe is higher than the binding energy of Cr, the latest can be ionized by this energy leading to a diminished intensity, as shown in curve B. In the third example, in contrast to the previous case, Ni has a binding energy higher than the characteristic energy of Fe which may result in the ionization of Fe due to Ni where the intensity increases (enhancement). When the characteristic energies of the elements are very close, the ionization of the elements is less likely resulting in a curve close to A, as in the case of curve D [17].

1.4.2 Sample thickness

The relationship between matrix effects and sample thickness in X-ray Fluorescence (XRF) analysis is illustrated in Figure 1.10, showing a correlation between the intensity of characteristic lines of analyzed elements and their concentrations. The thickness of the sample can be distinguished between "thin", "intermediate thick" and "infinitely thick". For "thin" samples the intensity of characteristic radiation of analyte does not depend on matrix composition. However, in practice the sample is not infinitely thin, and the infinitely thick sample model should be considered, where the intensity of characteristic radiation depends not only on an-

alyte concentration but also on full matrix composition [17]. For a sample emitting 99% of

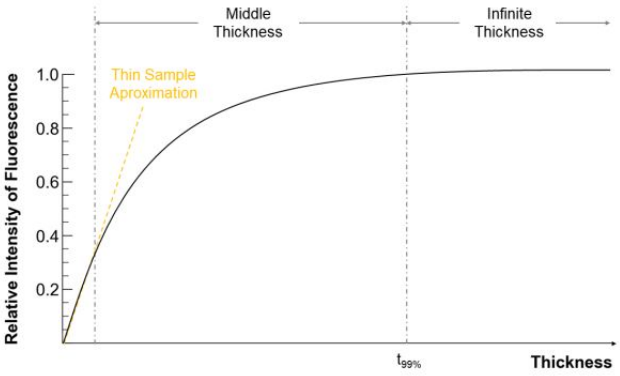

Figure 1.10: Relationship between fluorescence intensity, matrix effects and sample thickness in XRF analysis. Firstly a linear behavior is found in the thin sample, then the intermediate thickness and the infinite thickness zone.

fluorescent radiation, the infinite thickness is given by:

$$t_{99\%} = \frac{-\ln 1 - 0.99}{\rho[\mu(E_0)\csc(\phi_1) + \mu(E_i)\csc(\phi_2)]} \tag{1.22}$$

where ρ is the density of the sample (g/cm^3), $\mu(E_0)$ is the mass attenuation coefficient (in relation to incident radiation) (cm^2/g), $\mu(E_i)$ is the mass attenuation coefficient (in relation to element i) (cm^2/g), ϕ_1 is radiation incidence angle (rad), ϕ_2 is the fluorescent radiation angle (rad). Although matrix effects are neglected in thin samples, the sample's intensity depends on its thickness, fluorescence yield, atomic absorption coefficients, and transition probabilities. This data can be obtained by using certified standards with matrix effects similar to infinite thickness samples [18].

Chapter 2

State of Art

2.1 Analysis of Human Tissues Using EDXRF

X-ray Fluorescence techniques have been widely used for the detection and quantification of elements in a sample. As mentioned in the first chapter, trace elements play a role in the biological system and might stimulate malignant growth.

Magalhães et al. analyzed analyzed both normal and carcinoma tissues utilizing Energy Dispersive X-ray Fluorescence (EDXRF) and Total-reflection X-ray fluorescence (TXRF). They shown that the behaviour of the elements is tissue dependent, but a general increase in the levels of trace elements, as Fe, Cu, Zn, and even Br appears in the context of breast carcinoma [19, 20].

In a study performed by Ensina et al., it was used μEDXRF and two different methods of quantification were compared - Fundamental Parameters Method (FPM) and the External Standard Method ESM - after the determination of the dark matrix. One of the conclusion drawn was that the FPM approach rendered much more precise results, as the uncertainty is much lower than the ESM approach. This discrepancy is likely due to the FPM approach accounting for the influence of other analyte elements in the quantification, while the calibration curve-based ESM method does not consider matrix effects. Furthemore, variations were observed in samples containing lighter elements such as P, S, and K, which aligns with expectations given the significance of matrix effects, especially concerning self-absorption effects [21].

Machado et al. [22] applied the external standard calibration approach in the quantitative determination of elemental concentration in human, using the μEDXRF system M4 Tornado - Bruker. In this study, several calibration curves with the combination of two sets of CRMs, one of animal tissues CRMs and other one of plant leaves CRMs, were modeled, aiming to improve the accuracy of quantitative determinations of elements present in human tissues by XRF spectrometry. This improved approach was tested on paired samples of normal and tumour human tissue and all data was analysed using the advanced spectra processing tools of ROOT [23]. Reference samples were shown to be more accurate when used collectively than when used separately and despite the high heterogeneity of the samples, significant differences in the elemental concentration of low-Z elements, like K, were discovered. However, for some well-known trace elements like Fe and Zn there was not seen any significant variations. Also Carvalho et al. [24] quantified the concentrations of Fe, Cu, and Zn in paired tissues (normal and tumoral) of the lung using μ-XRF with the external standard method and detected an increase in Cu and a decrease in Fe and Zn in tumor tissues.

2.2 Formalin-Fixed Paraffin-Embedded Tissues

FFPE is one of the most employed fixation techniques in the medical field. In a study by Paunesku et al. [25], it was reported that previous investigations had confirmed the effective preservation of tissue morphology by FFPE, rendering it suitable for quantitative element analysis.

However, recent studies have unveiled that formalin can exert an influence on trace elements in tissues. Pessanha et al. [26] reported outcomes indicating a sharp decrease in Cl and K content within tissues after a two-day formalin fixation, with these elements being transferred to the formalin solution. Conversely, an accumulation of P within the tissue was observed, potentially attributed to the buffered formalin solution. However, no significant alterations were noticed in the case of S, Ca, Cu, Fe, and Zn.

Wróbel et al. [27] assessed the consistency of elemental composition changes induced by formalin fixation followed by paraffin embedding (FFPE). They compared the quantification of trace elements in lyophilized and FFPE-processed tissues using Total Reflection X-Ray Fluorescence (TXRF). Their findings indicated that the statistical dispersion for the elements remained below 30%, thereby opening the possibility for the analysis of extensive archival tissue populations.

Pessanha et al. in a recent work presented a methodology for the non-destructive elemental determination of FFPE human tissue samples based on the Fundamental Parameters method for the quantification of μEDXRF area scans. This methodology intended to overcome the determination of the dark matrix composition of the biopsied sample, evaluating different compositions using varying combinations of H, C, N and O. The final results showed distinctive biomarkers for breast and for colon: there was a significant increase of P, S, K and Fe in both tissues, while a significant increase of Ca an Zn concentrations was also determined for breast tumour samples [28].

Recognizing the susceptibility of certain elements (P, Cl, and K) to formalin fixation, and the lack of significant alterations for others (S, Ca, Cu, Fe, Zn, and Br), precise quantification of trace elements in FFPE samples, analyzed through EDXRF, becomes essential to further investigate tissues collected daily in hospitals. Given the significant impact of matrix effects for this spectroscopy technique, and the matrix alteration of paraffin embedding process, the development of a parametrization curve for elements concentration based on lyophilized pellet and FFPE samples is required to address this task effectively.

Chapter 3

Instrumentation and Methods

The study of the samples has been carried on using three different XRF systems in order to perform a more detailed analysis and extract more information from the tissues exploiting the different features of the spectrometers. In this chapter these instruments are described, highlighting their main working differences, in particular the tube excitation, geometry and spot size of investigation.

3.1 μ-EDXRF

Micro X-ray Fluorescence (μ-XRF) is an elementary analysis technique that allows point analysis with a diameter of less than hundreds of micrometers, using direct X-ray tube excitation to induce characteristic radiation emission of a sample.

Narrowing of the X-ray beam

The narrowing of the incident radiation beam can be done by collimators, mono-capillary or poly-capillary tubes (Figure 3.1a). Collimators limit the beam by absorption, while optical systems limit it by total reflection without decreasing the beam intensity. In the capillaries there is a high concentration of incident radiation, making the most of having a greater intensity at the point of analysis. Poly-capillary lens are made up of numerous hollow glass tubes with diameters less than 2 μm that through multiple total reflections focus the beam on an area of less than 100 μm. However, also the type of tube plays a role here, especially in the high brilliance required by μ-XRF, requiring small sized sources. This can be obtained using *side window tubes*, due to its geometry and its electrons emission from filaments like coils or tips, while *end*

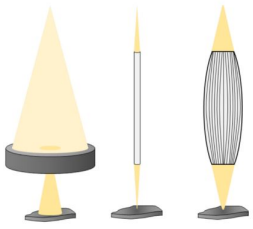

(a) Representation of a collimator, a mono-capillary and poly-capillary tube.

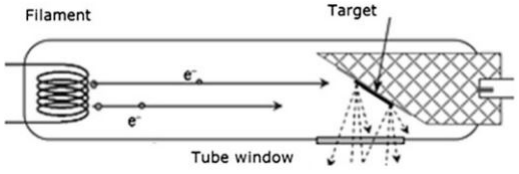

(b) Graphics of a side window X-ray tube, from [7].

Figure 3.1: Representation of collimators and capillary concentrators (left) and of a side window tube (right).

window tube and *transmission window tube* irradiate larger areas. The emitted radiation exits the tube by a window and it is possible to focus the electrons on a defined target area, like a line or a small spot [7]. A representation of this type of tube is Figure 3.1b.

Filters

The usage of filters enables an improvement in the peak-to-background ratio by lowering the bremsstrahlung radiation [16]. Depending on the emission energies, the choice of the filtering materials and their thickness may change. Filters are located at the exit of the X-ray tube, between the source and the sample, to absorb a certain range of energies, reducing the impact of the incident X-ray spectrum. In this instance, looking at substances that emit X-rays between 2 keV and 22 keV, and acquiring spectra of light elements, filters are applied enabling the removal of the L lines from the Rh X-ray tube and improving the sensitivity of the detection.

3.1.1 Bruker M4 Tornado

For this work Bruker M4 Tornado was used as μ-EDXRF spectrometer. It is composed by side window peltier-cooled Rh X-ray tube with a Be window to collect incident X-rays. A poly-capillary X-ray optics narrows the beam at a spot size of 25 μm for Mo-Kα radiation, which is then collected in a *XFlash 6-30* detector. The software used for the control of the spectrometer is *MQuant*, an in-built software of the M4 TORNADO system. Through the software it is possible to control, among the others, the area or spot to analyse, what filter to use, the time of the measurement, the parameters of the X-ray tube and the positioning of the sample. To set the position of the sample and the spot under investigation, Tornado is equipped with video cameras for real-time image transmission [29]:

- a camera in the sample chamber door that allows an overview of the sample in the chamber;
- a camera delivering an image of approximately 14 mm x 11 mm for orientation on the sample;
- a camera delivering an image of approximately 1.4 mm x 1.1 mm for the final positioning of the measuring spot.

For this study two different configurations have been used, reported in Table 3.1.1.

Excitation Parameters	**Configuration A**	**Configuration B**
Tube anode	Rh	
Filter	12.5 μm of Al	100 μm of Al, 25 μm of Ti
Tube excitation	50 kV, 300 μA	50 kV, 400 μA
Vacuum	not used	20 mBar
Acquisition Time	120 s	120 s
Acquisition spot	25 μm point size	

3.2 Triaxial EDXRF

EDXRF spectrometers assembled with orthogonal triaxial geometry between the X-ray tube, the secondary target, the sample and the detector (Figure 3.2) lessen the background of the measured spectra by reducing significantly the Bremsstrahlung produced in the tube through

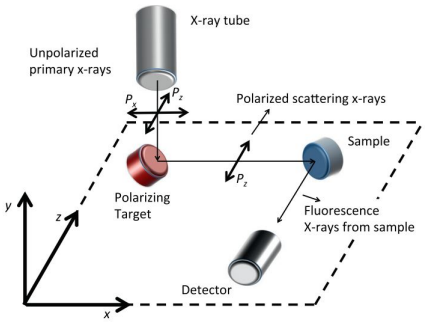

Figure 3.2: Representation of the geometrical orthogonal triaxial set up used, from [30].

polarization in the secondary target and in the sample. As mentioned in the first chapter, it is possible to polarize a transverse wave when it strikes a surface with the proper Brewer's angle. Consequently, a practically monochromatic excitation energy is obtained. In this way, a better peak-background ratio can be obtained compared to similar devices, improving the detection limits and leading to superior sensitivity. In order to assure the 90° angle between the radiation interacting with the sample and characteristic radiation reaching the detector, the use of collimators is inevitable. This comes along with the disadvantage of reducing even more the beam's intensity. This compromise has to be made between the collimator apertures and the intensity of the resulting spectra [14]. In Table 3.2.2 are stored the information of the two instruments and how they were set for the measurements.

3.2.1 Benchtop system

As a main triaxial EDXRF system a self-constructed water-cooled spectrometer has been used, consisting of a commercial X-ray tube with a W anode (Philips PW 2184) operated at 50 kV and 20 mA irradiating a Mo secondary target placed at a 90° angle with the sample. With this triaxial arrangement the bremsstrahlung radiation from the X-ray tube anode excites the characteristic lines of the secondary target (17.44 keV for Kα, 19.60 keV for Kβ), which will irradiate the sample. Both the X-ray beam emitted by the secondary target and the sample are collimated throughout two silver apertures. The specificities of the analized samples required the secondary target beam to be further collimated. This was obtained by an additional collimator of 2 mm of diameter. The beam shape was measured using a knife edge of Cu (Figure 3.3), resulting in an ellipse with a major horizontal axis of (2.44 $\pm$ 0.05) mm and minor vertical axis of (2.39 $\pm$ 0.05) mm. The acquisition of the spectra was controlled by the software *ProSpect*, which directed the SDD *VIRTUS H50* used by this spectrometer.

3.2.2 Portable system

The portable triaxial EDXRF system used is composed by a sided window X-ray tube with a Mo anode, (OXFORD XTF5011), working at 50 kV and 1 mA, and a changeable secondary target. The two used secondary targets are Yttium, with the characteristic lines at 14.931 keV for Kα and 16.731 keV for Kβ, and Germanium, with the characteristic lines at 9.874 keV for Kα and 10.979 keV for Kβ. This X-ray tube is still considered a low-power although it requires additional cooling performed by a fan and temperature monitoring. The spot size is ellipse shaped with a major axis of approximately 1.7 cm and minor axis of 1.2 cm [14]. Although the beam shape is larger than the benchtop system described above, in this case the beam was left

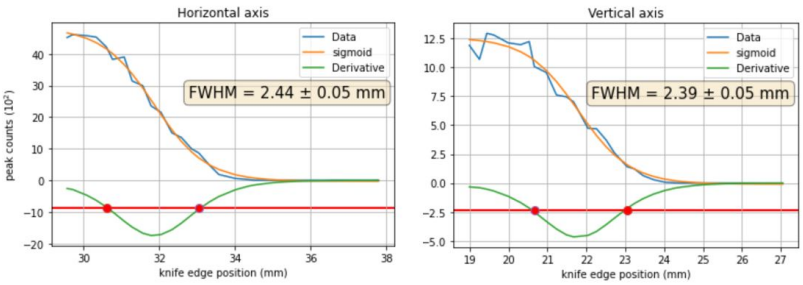

Figure 3.3: Plots of the Cu intensity peaks as a function of the distance from the knife edge both in the horizontal and vertical direction. The data was fitted to a Sigmoid function, its the derivative was calculated and the full width at half maximum (FWHM) of the derivative was used to determine the beam width.

at its original size to prevent the reduction of its intensity. The detector used is a *Vortex 60EX*, controlled by the software *PIspec*.

Excitation Parameters	**Benchtop**	**Portable**	
Tube anode	W	Mo	Mo
Secondary Target	Mo	Y	Ge
Tube excitation	50 kV, 20 mA	50 kV, 1 mA	50 kV, 1 mA
Acquisition Time	750 s	500 s	1500 s
Acquisition ellipse spot	2.44 mm, 2.39 mm	1.7 cm, 1.2 cm	

3.3 Detectors

The different spectrometers described in this chapter differ in the SDD used, the main differences are reported in Table 3.3.

Detector Features	**Tornado**	**Benchtop**	**Portable**
Name and model	XFlash 6-30	VITUS, H50	Vortex, 60EX
Sensitive area	30 mm^2	50 mm^2	50 mm^2
Resolution	145 eV	129 eV	160 eV
Be window	8.0 μm	12.5 μm	25.0 μm

Due to this differences, also detector limits vary from one system to the other. Inspecting the samples by the three of them gives complementary information.

3.4 Spectra Analysis

The commercial software *bAxil*, Analysis of X-ray spectra by Iterative Least squares method, from *BrightSpec*, has been adopted for the analysis and deconvolution of the acquired spectra. It analyzes any energy-dispersive X-ray spectrum, independently of its excitation and detection technology, thus it is suitable for the analysis of spectra coming both from triaxial EDXRF and μ-EDXRF. It performs the background removal and the fitting of the required peaks by building a mathematical model to describe the recorded experimental data. This is performed starting from the user selection of:

- the region of interest (ROI) on the spectrum,

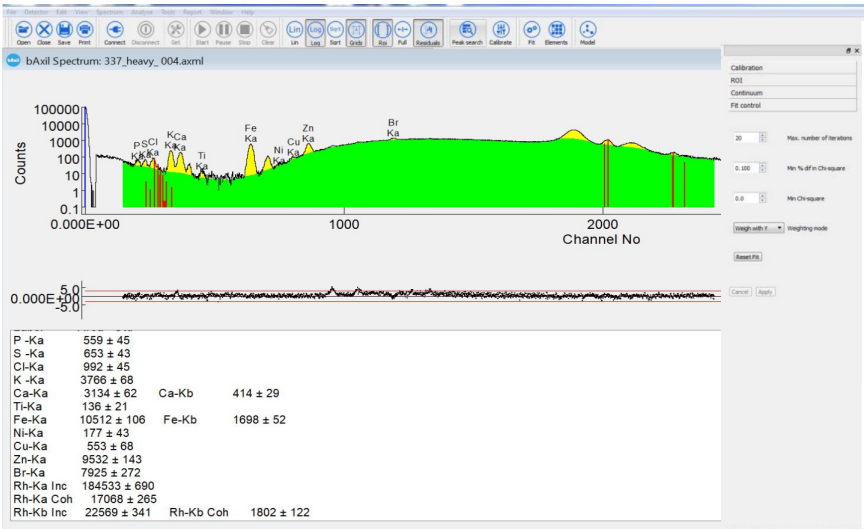

Figure 3.4: Example of dashboard of *bAxil* on a sample spectrum acquired by Tornado, reporting the spectrum fitted with the background removal, the residuals and the values of the peaks' intensities.

- the continuum (background) compensation algorithm,
- the identification and selection of the X-ray lines (peaks),
- the values for energy calibration parameters of the spectrometer.

The model parameters are optimized by means of non-linear least squares method, using a modified Marquardt algorithm to minimize the sum of differences (χ^2) between the experimental data and the established mathematical model [31]. The software uses also the geometry setup, from which depend the energy and intensity of the Compton peak, to fit properly the Coherent and Incoherent excitation peaks. The peak shape functions implemented are *Gaussian* and *Voight profile*, and escape peaks can also be taken into account. Each individual peak can have its own peak shape, even different from the other [32].

For the analysis of the spectra, all the peaks were fitted by *Gaussian* shape, the energy calibration of the three spectrometers were build using Ca Kα and Kβ peaks along with the coherent Kα and Kβ excitation peaks: Rh for Tornado, Mo for the benchtop, and Ge and Y for the portable triaxial system. Subsequently, the process of background removal was executed using the proprietary *Numerical Filter* algorithm, which is owned by the creators of *bAxil*.

Finally, the software requires a *.txt* spectrum file composed only by a column reporting the counts per each channel. To satisfy this requirement, the raw spectra files coming from the spectrometers had been adapted by a Python script for the removal of the header.

Chapter 4

Samples and Dataset

In this chapter are described the analyzed samples, mainly the sets of CRM pellets for the quantification and the tissues under investigation. At the end, the data acquisition in the three spectrometers is reported.

4.1 Tissue Dataset

In this section, the sets of samples used in this thesis are presented. Three sample sets were used due to the scarcity of biological material and the need to optimize the calibration models. Tissues were collected from surgical procedures at *Instituto Português de Oncologia de Lisboa Francisco Gentil* (IPO) and at *NOVA Medical School* (NMS). Every tissue sample was collected from different patients that have signed an informed consent to authorize their collection for research. All of the sets are caracterized by paired samples of a portion fixed in formalin freeze-dried in pellet (FF) and a portion embedded in a FFPE block:

- NMS samples are 6 samples of 6 different organs (ascending colon, bladder, heart, liver, lung and stomach) excised from a female corpse from Cadaveric Donation Office, Department of Anatomy, NMS. Samples were harvest in May 2020.
- IPO samples from June 2020 are 6 samples of different organs from different patients (colon, stomach and spleen).
- IPO samples from June 2023 are 7 healthy tissues of different organs of different patients (breast, skin, colon and goiter).

4.1.1 FFPE block preparation

Paraffin embedding of formalin fixed tissues is a common and practical modality to store and preserve biological samples from degradation. As described in the first chapter, after the intervention is performed the tissue is immersed into formalin, then a progressive dehydration prepares the sample to the suitable condition to be embedded in paraffin. This process, for the samples under study, has been carried on at IPO and NMS. The used FFPE blocks are reported in Figure 4.1.

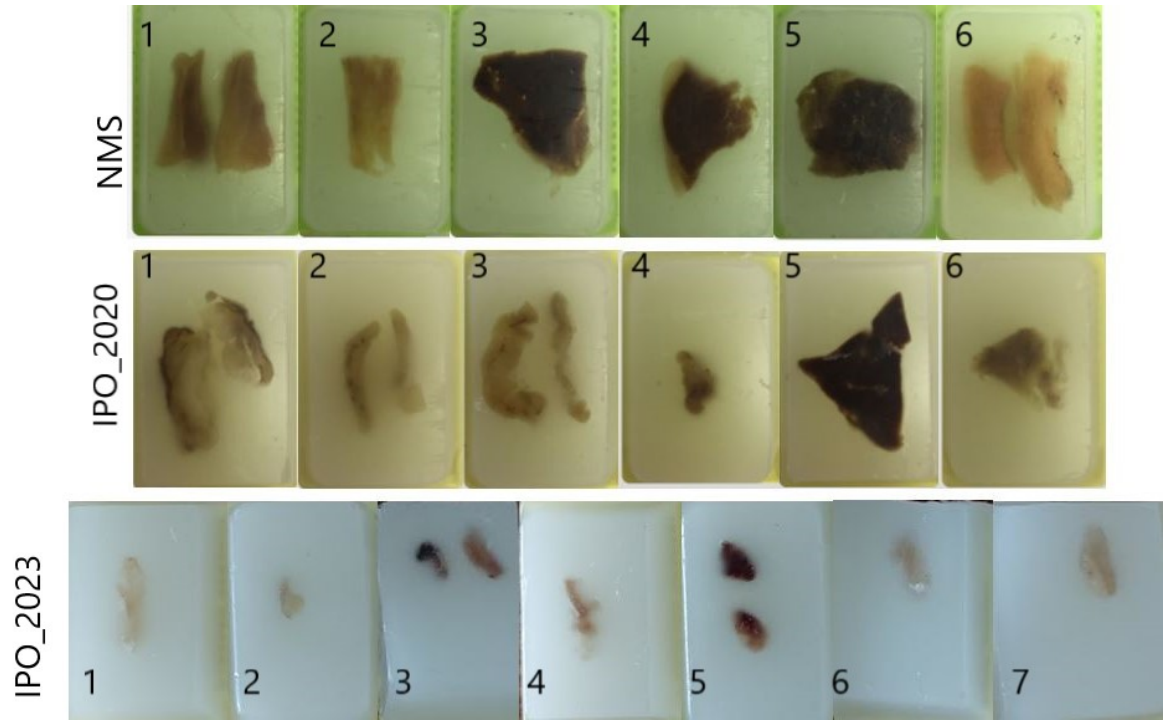

Figure 4.1: Photographs of NMS and IPO FFPE Samples collected in 2020 and IPO FFPE Samples collected in 2023.

4.1.2 Pellet preparation

Heterogeneity of samples can be a source of large systematic errors due to particle size and surface effects. To minimize these errors adequate preparations methods can be adopted. Regarding EDXRF, sample powdering followed by preparation of pressed pellets, ensure a homogeneous sample with a smooth surface and small enough grains [22].

The pellets from the datasets IPO_2020 and NMS came along with their paired FFPE blocks, while the ones of the dataset IPO_2023 were prepared by the author of this work following the same procedure of the previous ones. The tissues used to prepare the pellets were collected from IPO and while still immersed in formalin were moved to the LIBPhys laboratory of NOVA School of Science and Technology.

The samples were lyophilized at 10^{-3} mbar [A], grounded in a mortar [B] to obtain a fine powder and increase homogeneity of the sample. After this mechanical process, without adding any chemical treatment, the powder was pressed into pellets [C] of a diameter of 7 mm and at 1 ton of pressure [D]. Finally the pellets were sticked upon a Mylar film, secured by carbon tape and placed on a slide frame [E] (Figure 4.2). The sets used in 2020 for previous studies were pressed into larger pellets of a diameter of 15 mm and at 3 tons pressure. Unfortunately, due to the scarcity of biological tissue this size was not suitable for the newer samples.

4.2 CRMs Dataset

Two different sets were used to study the samples: the first one to study the dependency model of the mean-Z as a function of the X-ray tube excitation source Kα Compton-to-Rayleigh ratio and the second one to perform the quantification using the external quantification method. The first set consists of different proportions of reference materials of Hydroxyapatite HAp

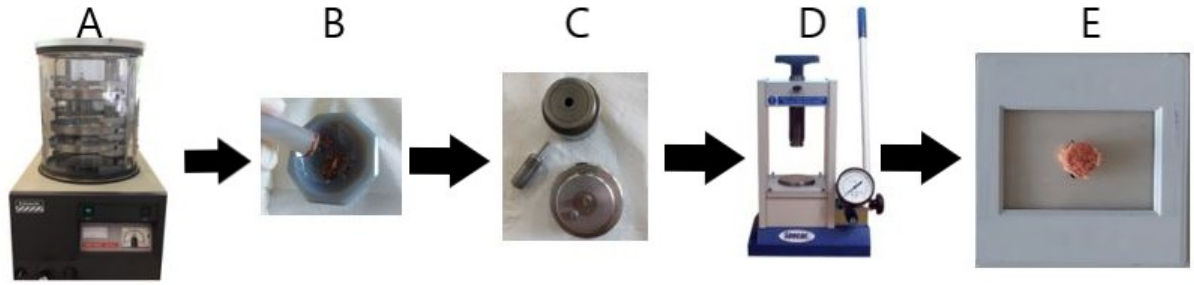

Figure 4.2: Pellet manufacturing for lyophilized samples.

$[Ca_{10}(PO_4)_6(OH)_2]$ (Sigma-Aldrich, lot #BCBS8492V), and Boric Acid HB $[H_3BO_3]$ (for conservation–restoration purposes), PMMA and a plain paraffin block, with an atomic number range of $5.2 < Z < 14$.

In order to build quantification curves for the external standard method, 12 animal and plant CRMs were used: NIST SRM 1577a Bovine Liver, NIST SRM 1566 Oyster Tissue, NIST SRM 1566b Oyster Tissue, IAEA MA-A-2 Fish Flesh Homogenate, NRC-CNRC TORT-2 Lobster Hepatopancreas Reference Material for Trace Metals, ERM-BB186 Pig Kidney, NRC – CNRC DORM-4 Fish Protein certified reference material for trace metals, NIST SRM 1571 Orchard Leaves, GBW 07603 Trace Elements in Bush Branches and Leaves, GBW 07604 Poplar Leaves, GBW 07605 Tea, NIST SRM 1575 Pine Needles. All CRMs were analysed as 15 mm diameter and 1 mm thick pressed pellets, glued on a Mylar film, and placed on a sample holder.

4.3 Data acquisition

The spectra acquisition of a sample depended on its dimension. CRMs pellets' size is suitable for all of the three spectrometers, while the dimension of the FFPE sample varies from sample to sample, as can be noticed in Figure 4.1. This does not present any constrain in the analysis performed using Tornado, while it becomes an issue in the analysis using the triaxial systems, due to the larger acquisition spots.

As a consequence the data acquisition was performed as follow:

- in the **portable triaxial system** (elliptical spot size of axis 1.7 cm, 1.2 cm) only the FFPE NMS_3, NMS_4 and NMS_5 were studied to investigate them using different exciting energies (from Yttrium and Germanium);
- in the **benchtop triaxial system** (elliptical spot size of axis 2.44 mm, 2.39 mm) all the NMS and IPO_2023 FFPE blocks were acquired. The set IPO_2020 was excluded because the positioning of the blocks in the sample holder presented some dimensional issues, which could be solved only by cutting the blocks to reduce their dimensions, as done with the set IPO_2023. The decision of acting only on set IPO_2023 is to be found in the purpose of the study: this set was not inherit from previous studies and the original FFPE block preservation was not a priority over its investigation in this spectrometer.
- in **Tornado M4** all the FFPE blocks were studied by spot size acquisition (down to 25 μm).

For what concerns the number of spectra per each sample, more spectra were acquired to guarantee that the analysis was the most representative as possible of the average composition

of the samples. The sample holder in both of the triaxial systems, allowed up three different spot acquisitions per each pellet, while in the μEDXRF it has been chosen to select 10 points to acquire per each sample and per each CRM.

4.3.1 Acquisition Time

The acquisition live time was set differently in each spectrometer, and in the portable triaxial system it differed also depending on the secondary target used. The choice of the time was based on the consideration that the uncertainty in the measurement of a peak in an XRF spectrum is proportional to the square root of the number of counts in the peak. This means that the uncertainty can be reduced by increasing the number of counts. However, there is a trade-off between acquisition time and uncertainty. The longer the data is acquired, the more counts the spectrum will get, and the lower the uncertainty will be. However, the acquisition time also increases the risk of some kind of changes that could affect the measurement, mainly the rising temperature of the X-ray tube and sample drift.

In this study, it was used the Fe Kα peak to estimate the uncertainty in the measurements, by the formula derived from the Poisson distribution:

$$uncertainty = \frac{\sqrt{counts}}{counts} \tag{4.1}$$

The result of the calculation for the used times (120 s in Tornado M4, 750 s in the benchtop triaxial, 500 s for Y, and 1250 s for Ge in the portable system) is less than 10%, indicating that the uncertainty in the measurement is less than 10% of the peak height, a good level of uncertainty for most applications.

Chapter 5

Results

In this chapter, the results of this study are presented. Firstly, the treatment of the acquired spectra is reported, followed by the results of the Compton-to-Rayleigh ratio of the samples and their elemental quantification. Finally the quantification of FFPE is obtained by a parametrization of the intensity peaks between the tissues in pellets and blocks. The results obtained from the Tornado configurations and the triaxial system are compared at the very end.

5.1 Data treatment

The spectra acquired were analyzed by *bAxil* to obtain the net intensities of peaks. The large amount of data was stored and processed in *Excel* files, and finally plotted and analyzed by *OriginPro 2023*. In the Benchtop triaxial spectrometer 3 spectra per each sample were acquired, while in Tornado 10 points were chosen in each sample to have a better representation of its average composition. In order to minimize the fluctuations among the same sample, for each spectrum the Kα element peak intensities was normalized by the Compton-to-Rayleigh ratio, as already been performed in literature to reduce matrix effects [33]. The Compton-to-Rayleigh ratio is obtained by dividing the intensity of the Compton Kα peak by the Rayleigh Kα peak corespondent to the characteristic radiation of the X-Ray source of the spectrometer, in this case Rh for Tornado, Mo for the benchtop and Ge or Y for the portable triaxial, which are shown in Figure 5.1. Subsequently, having less spectra in the triaxial system, the mean value of the normalized intensity was calculated per each sample, and the maximum deviation from the mean was used as uncertainty. While for the samples acquired by Tornado, having more spectra, the standard deviation was used. The analysis performed took into account the uncertainties both in X and Y-axis (for the quantification and parametrization curves) or only in X (for the Compton-to-Rayleigh ratio versus the mean Z), since they are measured quantities. The algorithms used to fit the data were in the first case the *Deming linear regression*, while in the second case *Orthogonal Distance Regression* in exponential or fractional functions (the ones in Figures 5.2 and 5.3). The results are shown as the calculated value from the fit function and the associated uncertainty is the error propagation through partial derivatives:

$$\delta y = \sqrt{\left(\frac{\partial y}{\partial A}\delta A\right)^2 + \left(\frac{\partial y}{\partial A}\delta A\right)^2 + \left(\frac{\partial y}{\partial B}\delta B\right)^2} \tag{5.1}$$

where A and B are the intercept and slope of the *Deming linear regression*, and x the measured value. Regarding the evaluation of the fit performed, the *Pearson's r* was used in the Deming regressions, while the reduced chi-squared test was adopted for the mean-Z curves.

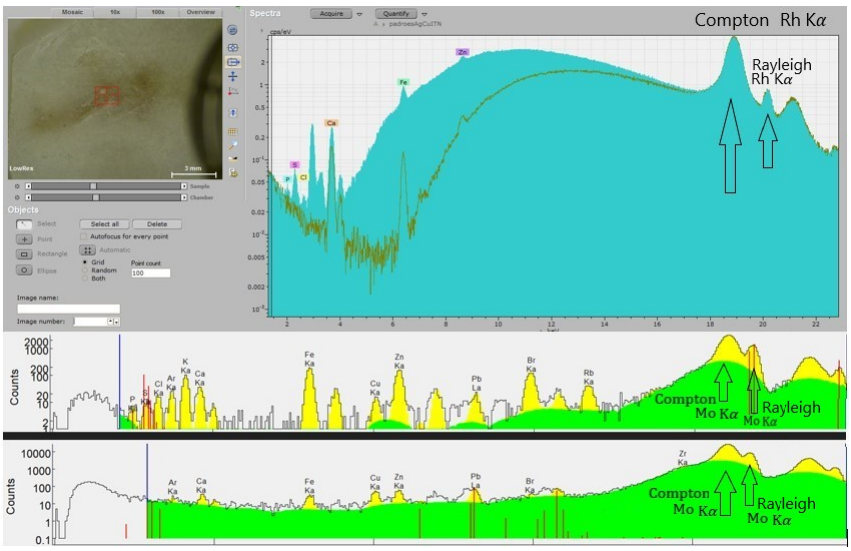

Figure 5.1: Example of spectra of the sample IPO_23_4. In the upper part the dashboard of *MQuant* with the internal camera to focus on the sample is shown. The blue spectra was acquired in configuration A, while the green-lined one in configuration B. The Rh Kα Compton and Rayleigh peaks are highlighted. The central and bottom spectra are respectively from the pellet and the FFPE block of the same sample, analyzed in *bAxil*, acquired by the Triaxial spectrometer. Mo Kα Compton and Rayleigh peaks are pointed out.

5.2 Compton-to-Rayleigh ratio and samples' matrix

As mentioned in the first chapter in section 1.2.2, the Compton and Rayleigh cross sections depend on the atomic number of the target. The Compton-to-Rayleigh ratio can provide important information regarding the average atomic number of the sample under investigation, hence its matrix. The very specific dependence on the average atomic number makes the Compton-to-Rayleigh ratio an easy to compute analytical feature, which can be extracted from the XRF spectra, particularly for scattering peaks at higher energies, as the tube excitation ones. The synthesis of a calibration curve Compton-to-Rayleigh intensity ratio versus average atomic number can gain a special importance when samples of partially unknown compositions, as human tissues, are investigated under the same geometrical conditions and at the same energy [34]. For each of the four excitation energies used in the spectrometers (Rh, Mo, Y and Ge) these curves have been obtained by fitting the plotted values of the set of reference materials, with known mean Z, of Hydroxyapatite, PMMA and plain paraffin block, as reported in the previous chapter (see section 4.2). The fit function, receiving in input the Compton-to-Rayleigh ratio, calculated per each sample by averaging its spectra, returned as output its mean Z. Per each CRM, used for the quantification, and per each the tissue samples of this study, the inferred mean Z was plotted to graphically see its distribution. From the plots the following considerations can be made:

- the plots of Tornado, in both configurations, and of the Benchtop system (Figure 5.3) show that the External Quantification Method is suitable for the tissues in the pellets form since their mean Z lay in the same area of the CRMs' ones;
- on the other hand, the paraffin embedding of FFPE block alters the matrix composition, lowering their mean Z and hindering the External quantification method.
- Finally, regarding the three samples studied in the triaxial spectrometers, the inferred

mean Z are decreasing by increasing the excitation energy used by the systems (Ge, Y and Mo). This could indicate that by increasing the energy of the X-ray beam, its penetration in the sample increases, and possibily reaches the paraffin beyond the tissue inside the block. This would determine a decrease of the inferred mean Z, due to its lighter matrix. However, these results are not conclusive, further assessments on the thickness of the tissue embedded in the block should be performed.

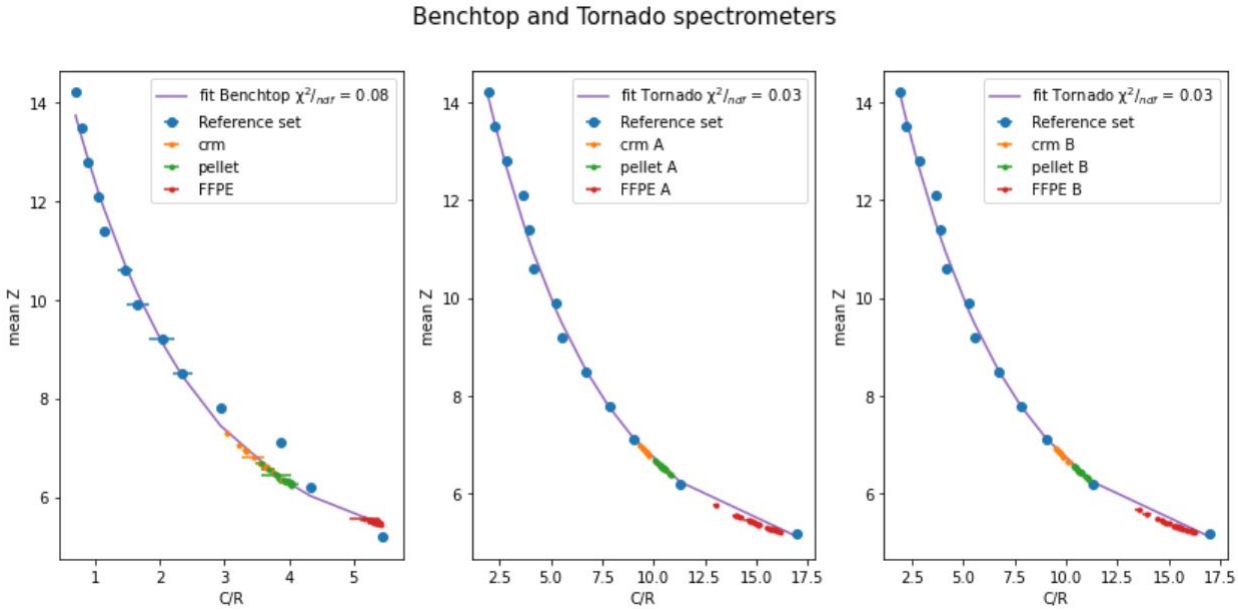

Figure 5.2: Plots of the Compton-to-Rayleigh ratio versus mean Z of the specimen for the Benchtop system and the two different configuration used in Tornado.

5.3 External Standard Method for elements quantification

As mentioned in the first chapter (section 1.4), the External Standard Method quantification can be used to quantify elements in sample with a matrix compatible with the CRMs. Following the study of Machado et al. [22] (see section 2.1), a total of 12 plant or animal CRMs, were used to build calibration curves per each element, knowing CRMs' concentrations and their associated uncertainty. The construction of the curves for each element of interest was performed by the Kα/Ratio and element concentration values, with their respective deviations and uncertainties. Using different excitation energies and filter configuration, the analyzed elements for Tornado in configuration *A* are S, Ca, Ti and Fe; in configuration *B*, which used a thicker filter, are S, Ca, Fe, Cu and Zn. Finally in the Benchtop triaxial system are Ca, Fe, Cu, Zn and Br. Per each spectrometer and its configuration a CRM of the set was excluded from the building of the curve and used to evaluate the method's validity and accuracy. Then the quantification of these elements in the pellets was performed and finally also in the FFPE, after the construction of the parametrization curves.

In the following paragraphs these steps, which can be visualized in Figure 5.4 are reported for the spectrometer Tornado, in both configurations, and for the Benchtop triaxial system.

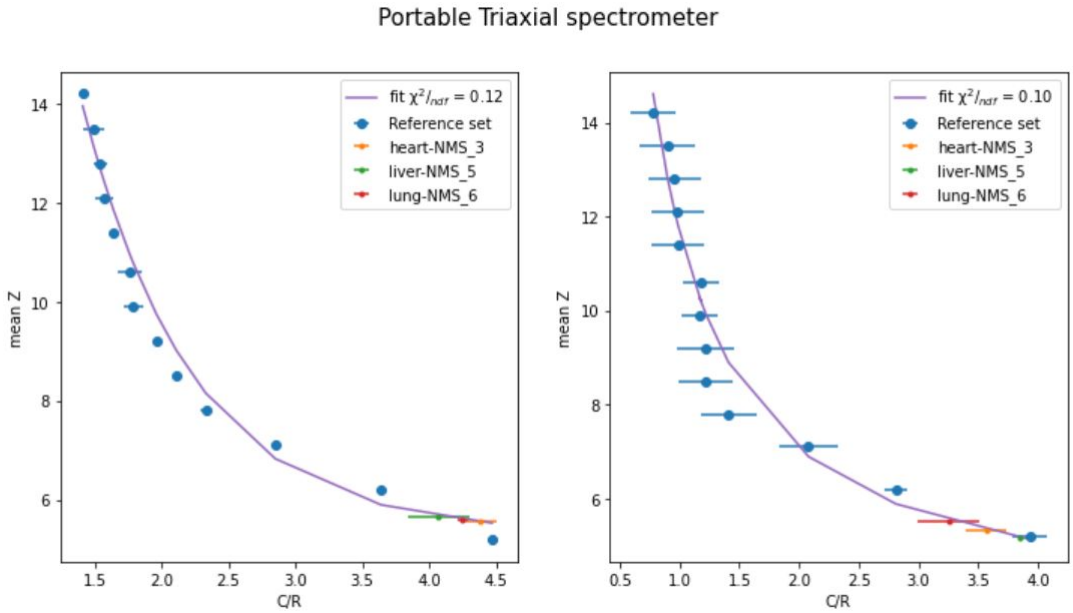

Figure 5.3: Plots of the Compton-to-Rayleigh ratio versus mean Z of the three FFPE blocks analyzed in the portable triaxial spectrometer.

5.3.1 Tornado Results

Elemental calibration curves

To validate the curves constructed using the CRMs, one of them was kept out and quantified starting from its normalized element peak and the obtained curve. For the elements Zn, Cu and Fe all of the elements of the set had certified values, while for S, Ca and Ti only 5, 9 and 4, respectively. The CRM *GBW 07604 Poplar Leaves* was used in configuration A, while *GBW 07603 Trace Elements in Bush Branches and Leaves* in configuration B. The results of the validation (all in in μg/g), the discrepancies with the reference value, and the equation of the curves are reported in Tables 5.1 and 5.2.

	CRM	Ref Value	Obtained value	% Δ	Equation
S	Poplar	$(3.3\pm0.7)\cdot10^2$	$(3.5\pm0.8)\cdot10^2$	7.1	$y=(-6\pm6)\cdot10^2$ μg/g$+(30\pm2)\cdot x$
Ca	Poplar	$(18\pm3)\cdot10^3$	$(20\pm2)\cdot10^3$	8.8	$y=(-3\pm6)\cdot10^2$ μg/g$+(1.4\pm0.1)\cdot x$
Ti	Poplar	20±5	20±50	11.1	$y=(-4\pm4)\cdot10^1$ μg/g$+(0.8\pm0.4)\cdot x$
Fe	Poplar	$(2.7\pm0.4)\cdot10^2$	$(2.7\pm0.6)\cdot10^2$	3.5	$y=(-13\pm5)\cdot10^1$ μg/g$+(0.21\pm0.02)\cdot x$

Table 5.1: Results of the validation of the quantification curves obtained for the spectrometer Tornado in configuration A using the CRM GBW 07604 Poplar Leaves. Per each element the reference value, the obtained value and their percentage discrepancy (Δ) is reported. The last column indicates the equation of the quantification curve.

For both configurations the discrepancies are below 10% and go over this value only for low concentration. However, it could be noticed that the best curve fit is found for the closer the intercept gets to 0, i.e., intercept ± incertainty closer to zero. For S this occurs in configuration A, while for Fe the intercept is smaller in configuration B. This finds an explanation considering that in A a lower Z filter (for light elements) is used, while in B a higher Z filter (for heavier elements) is adopted.

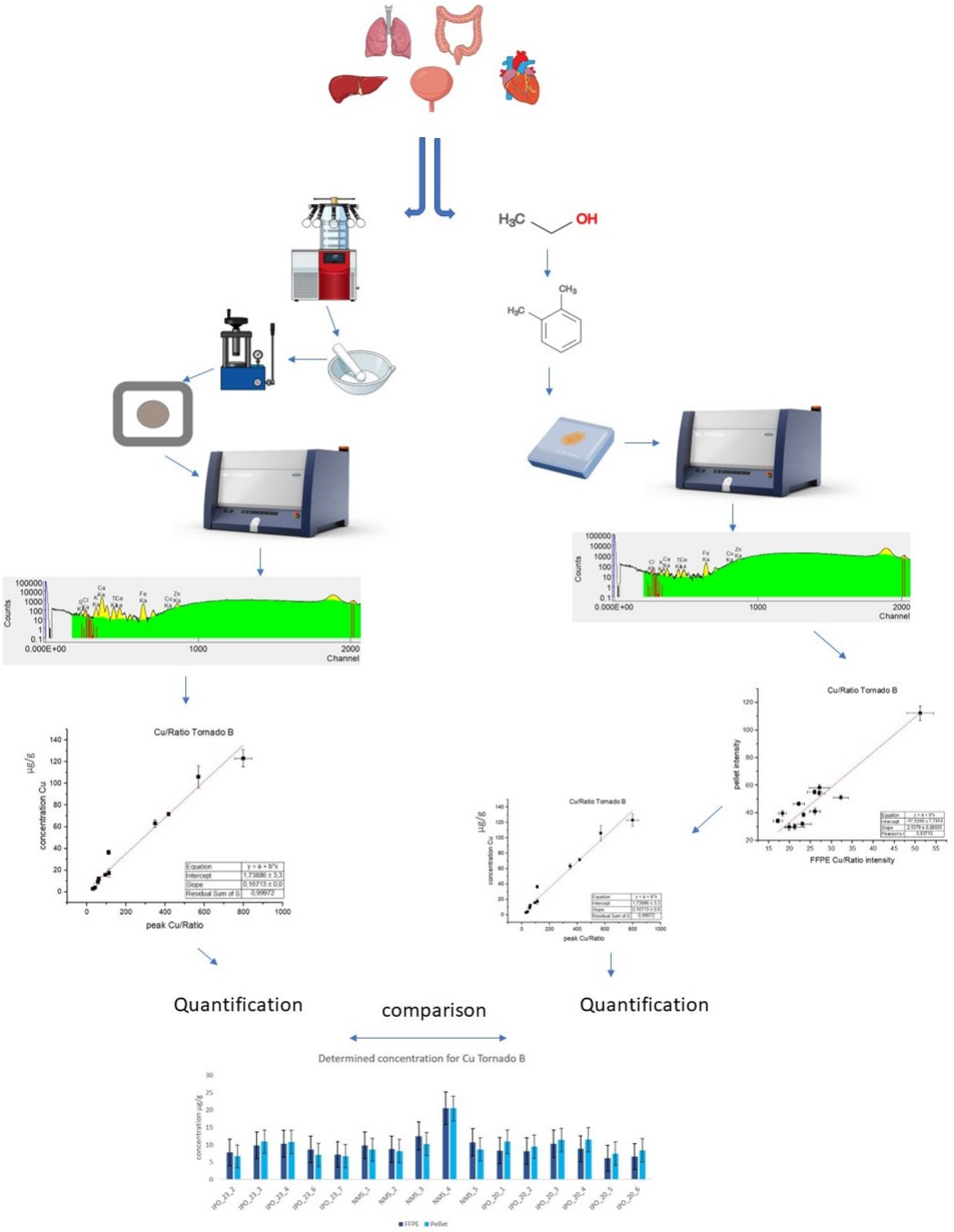

Figure 5.4: Representation of the steps of the analysis: firstly the biopsed tissue undergoes the formaline fixation; then a portion of it is processed into a pellet while the rest is store in FFPE block. The two are analyzed in the spectrometer, the spectra peaks are integrated and, in the case of the pellet, quantified directly using the quantification curve build using the CRMs. For the FFPE block the quantification requires a previous step of parametrization: the intensity of the block is translated into a *pellet intensity* by the parametrization curve and finally using this parametrized value it is quantified. At the very end the inferred concentration of the pellet and the FFPE block are compared.

	CRM	Ref Value	Obtained value	% Δ	Equation
S	Bush	$(7\pm1)\cdot10^3$	$(8\pm2)\cdot10^3$	2.4	$y=(-1\pm1)\cdot10^3\ \mu g/g+(12\pm2)\cdot10^2\cdot x$
Ca	Bush	$(1.7\pm0.2)\cdot10^4$	$(1.6\pm0.1)\cdot10^4$	4.1	$y=(-1\pm5)\cdot10^2\ \mu g/g+(6.7\pm0.3)\cdot x$
Fe	Bush	$(11\pm1)\cdot10^2$	$(10\pm1)\cdot10^2$	4.7	$y=(-8\pm4)\cdot10^1\ \mu g/g+(0.68\pm0.06)\cdot x$
Cu	Bush	7 ± 2	8 ± 3	16.4	$y=(2\pm3)\ \mu g/g+(0.17\pm0.01)\cdot x$
Zn	Bush	55 ± 8	$(6\pm1)\cdot10^1$	2.7	$y=(2\pm1)\cdot10^1\ \mu g/g+(0.140\pm0.003)\cdot x$

Table 5.2: Results of the validation of the quantification curves obtained for the spectrometer Tornado in configuration B using the CRM GBW 07603 Trace Elements in Bush Branches and Leaves. Per each element the reference value, the obtained value and their percentage discrepancy (Δ) is reported. The equation of the quantification curves are listed in last column.

Tissue quantification

The purpose of this work is to be able to quantify elements in FFPE tissue blocks. In order to do so a parametrization of the formalin embedding effects on the dark matrix needs to be performed. To achieve this, a parametrization curve between the normalized Kα peaks of the FFPE blocks and the mirrored tissues processed in pellets has been plotted per each element of interest of the two configurations. To validate these curves NMS_3 has served as control sample, in a validation process that followed the one for the quantification curves. The obtained intensity compared with the measured ones are shown in Figure 5.5.

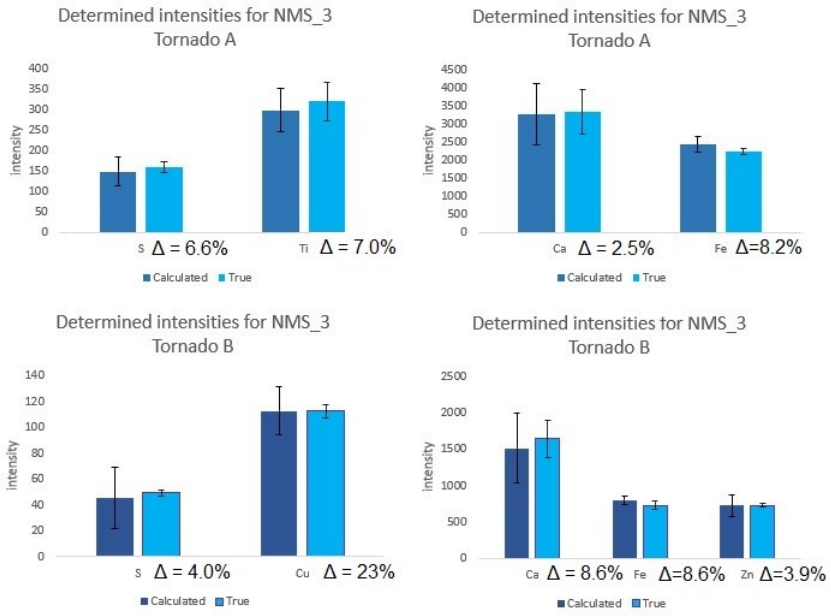

Figure 5.5: Plots of comparison between calculated and measured intensities and relative percentage discrepancies for the elements of interest of the sample NMS_3.

With this curves the intensities of the FFPE blocks had been transformed into *pellets intensities* and with them the quantification curves early described allowed to quantify the elements in the blocks. This process comes along with error propagation and the errors associated to the results are in most of the case not negligible. From Figure 5.6 to Figure 5.14 the two curves and the comparison between the concentration calculated for the tissues in pellets and in FFPE, for discepancies between the two forms smaller than 40%, are shown for both of the configurations. The equation of the parametrization curves are summarized in Tables 5.3 and 5.4.

Element	Equation	Pearson's r
S	$y=(3\pm3)\cdot10^1+(2.5\pm0.4)\cdot x$	0.875
Ca	$y=(-4\pm2)\cdot10^2+(9.8\pm0.8)\cdot x$	0.968
Ti	$y=(13\pm7)+(1.4\pm0.2)\cdot x$	0.947
Fe	$y=(9\pm2)\cdot10^2+(1.7\pm0.1)\cdot x$	0.976

Table 5.3: Results of the parametrization curves obtained for the spectrometer Tornado in configuration A. Per each element the equation of the curve and the Pearson's r value are reported.

Element	Equation	Pearson's r
S	$y=(-2\pm2)\cdot10^1+(3.4\pm0.8)\cdot x$	0.821
Ca	$y=(-5\pm2)\cdot10^2+(23\pm4)\cdot x$	0.882
Fe	$y=(2.4\pm0.4)\cdot10^2+(2.07\pm0.08)\cdot x$	0.988
Cu	$y=(-18\pm8)+(2.5\pm0.3)\cdot x$	0.937
Zn	$y=(-1.4\pm0.8)\cdot10^2+(3.7\pm0.5)\cdot x$	0.921

Table 5.4: Results of the parametrization curves obtained for the spectrometer Tornado in configuration B. Per each element the equation of the curve and the Pearson's r value are reported.

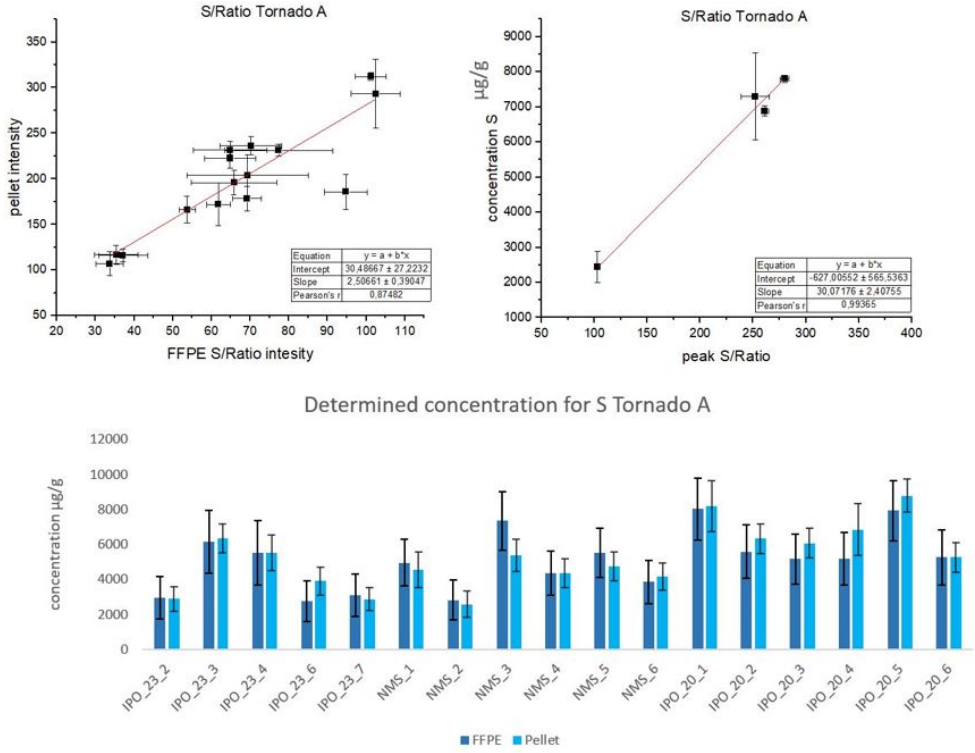

Figure 5.6: Analysis for S in configuration A. Up left: parametrization curve with Pearson's r = 0.875; up right: quantification curve with Pearson's r = 0.994. Bottom: plot of the calculated concentration for tissues in FFPE blocks and pellet.

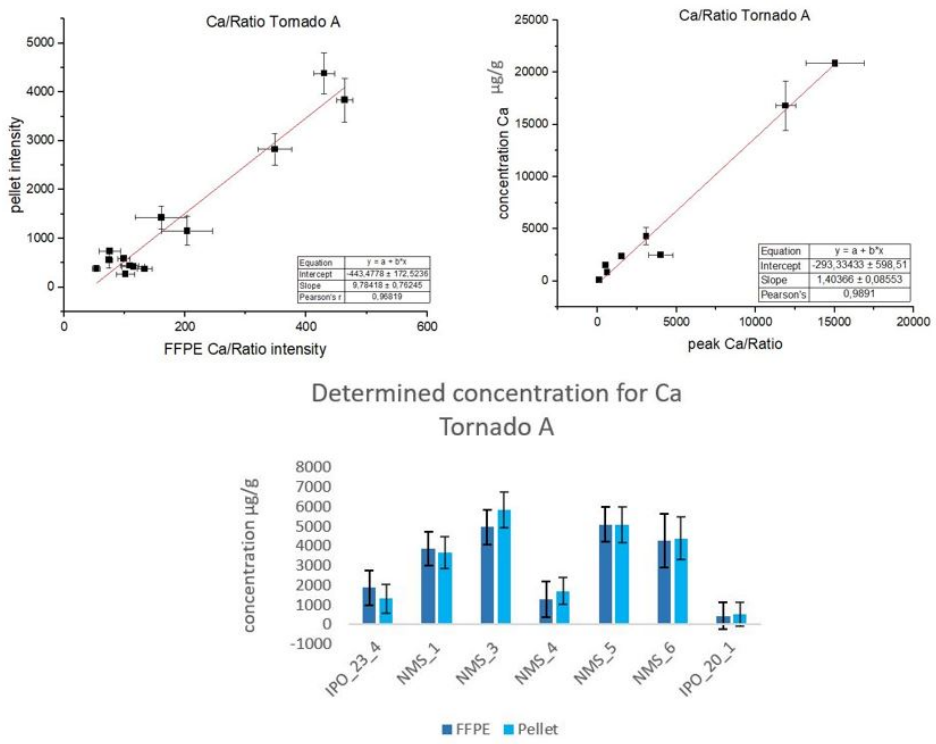

Figure 5.7: Analysis for Ca in configuration A. Up left: parametrization curve with Pearson's r = 0.968; up right: quantification curve with Pearson's r = 0.989. Bottom: plot of the calculated concentration for tissues in FFPE blocks and pellet.

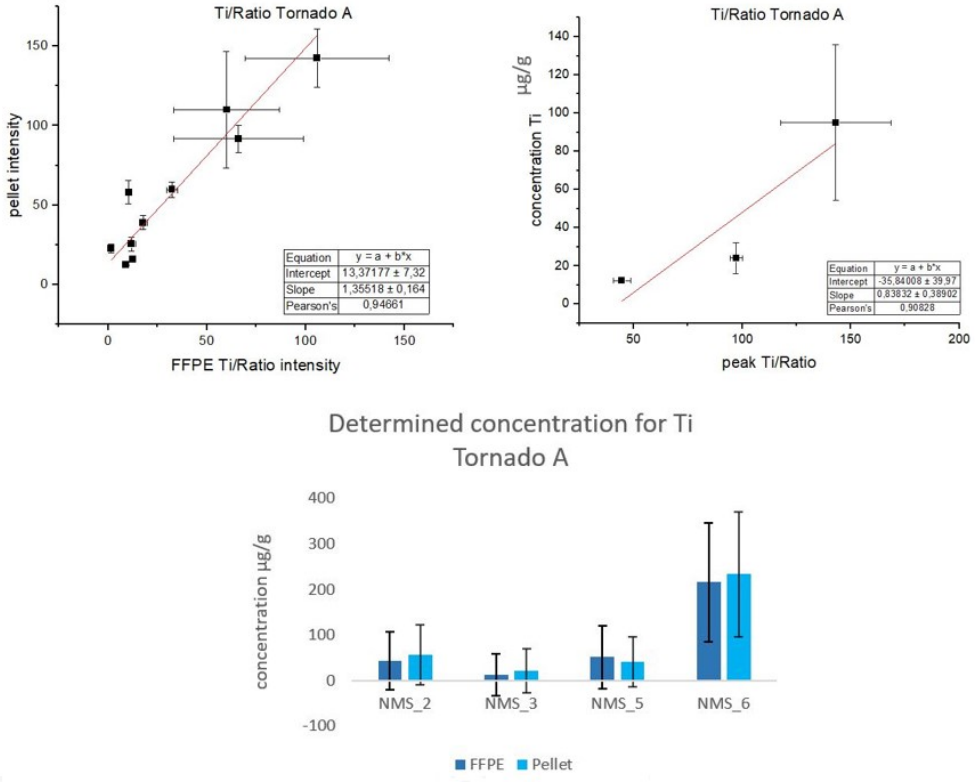

Figure 5.8: Analysis for Ti in configuration A. Up left: parametrization curve with Pearson's r = 0.947; up right: quantification curve with Pearson's r = 0.908. Bottom: plot of the calculated concentration for tissues in FFPE blocks and pellet.

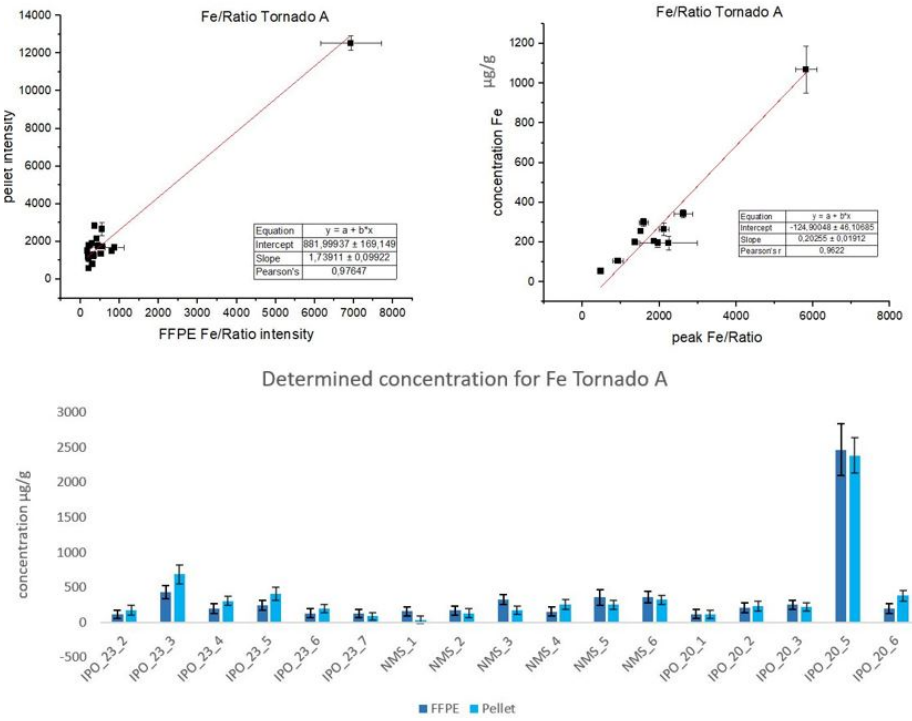

Figure 5.9: Analysis for Fe in configuration A. Up left: parametrization curve with Pearson's r = 0.976; up right: quantification curve with Pearson's r = 0.962. Bottom: plot of the calculated concentration for tissues in FFPE blocks and pellet.

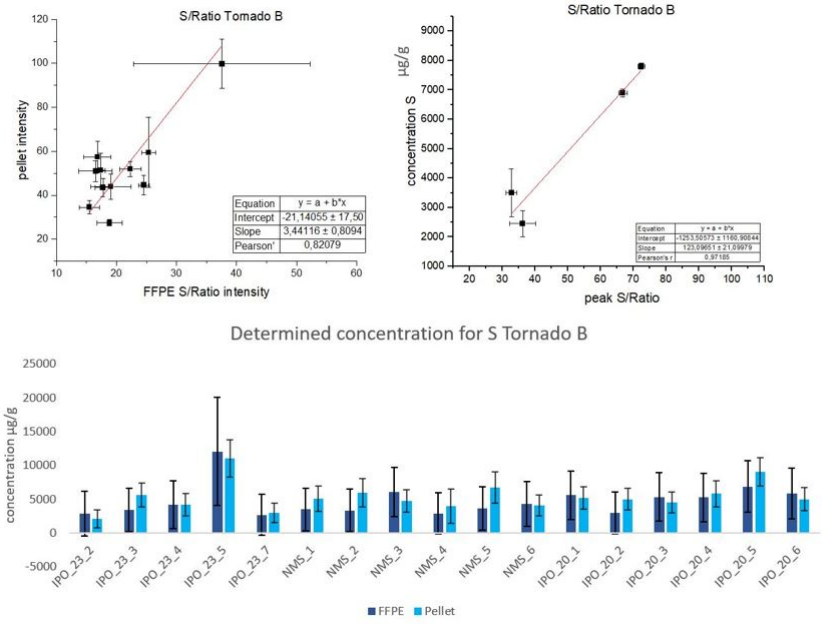

Figure 5.10: Analysis for S in configuration B. Up left: parametrization curve with Pearson's r = 0.821; up right: quantification curve with Pearson's r = 0.972. Bottom plot of the calculated concentration for tissues in FFPE blocks and pellet.

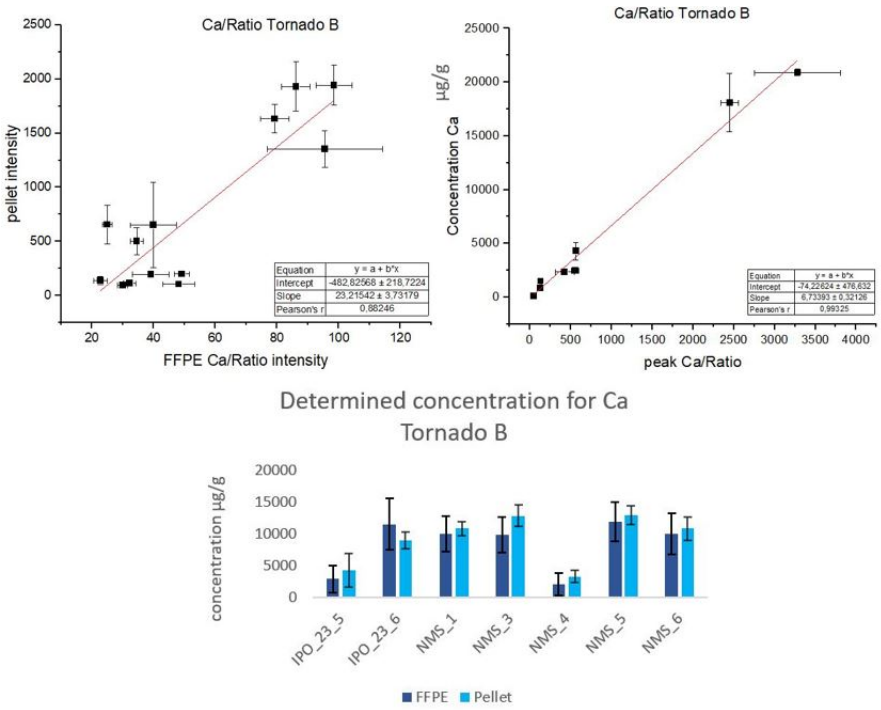

Figure 5.11: Analysis for Ca in configuration B. Up left parametrization curve with Pearson's r = 0.882; up right: quantification curve with Pearson's r = 0.993. Bottom: plot of the calculated concentration for tissues in FFPE blocks and pellet.

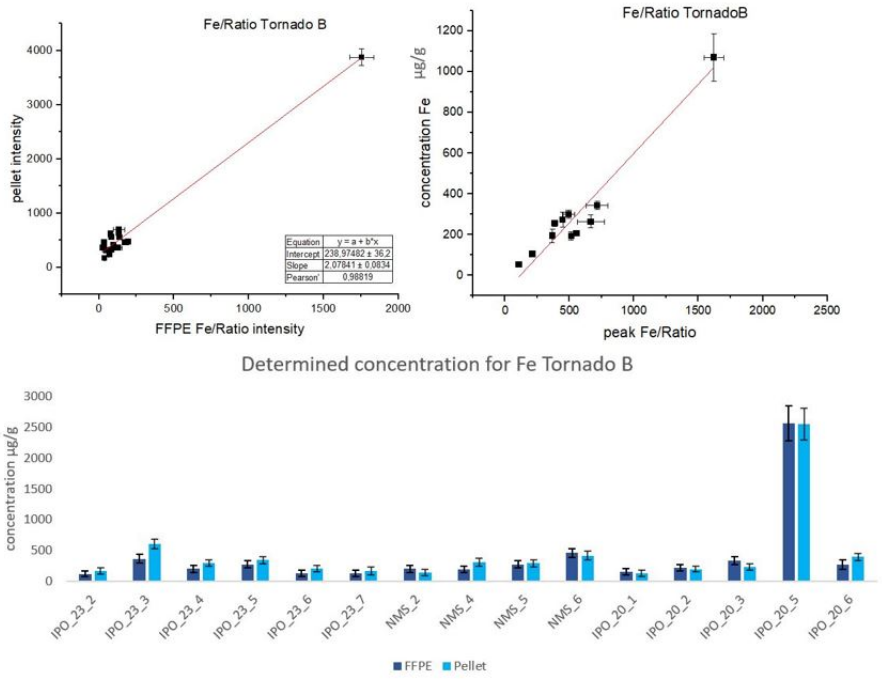

Figure 5.12: Analysis for Fe in configuration B. Up left: parametrization curve with Pearson's r = 0.988; up right: quantification curve with Pearson's r = 0.967. Bottom: plot of the calculated concentration for tissues in FFPE blocks and pellet.

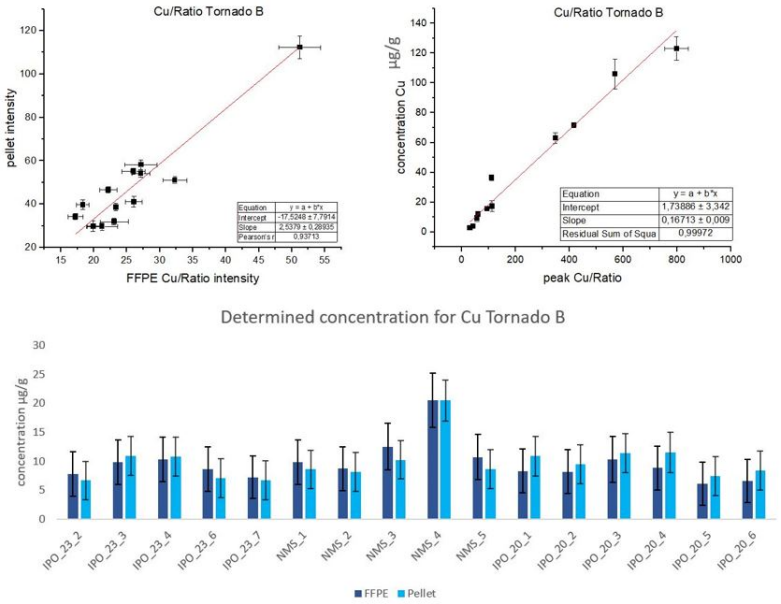

Figure 5.13: Analysis for Cu in configuration B. Up left: parametrization curve with Pearson's r = 0.937; up right: quantification curve with Pearson's r = 0.999. Bottom: plot of the calculated concentration for tissues in FFPE blocks and pellet.

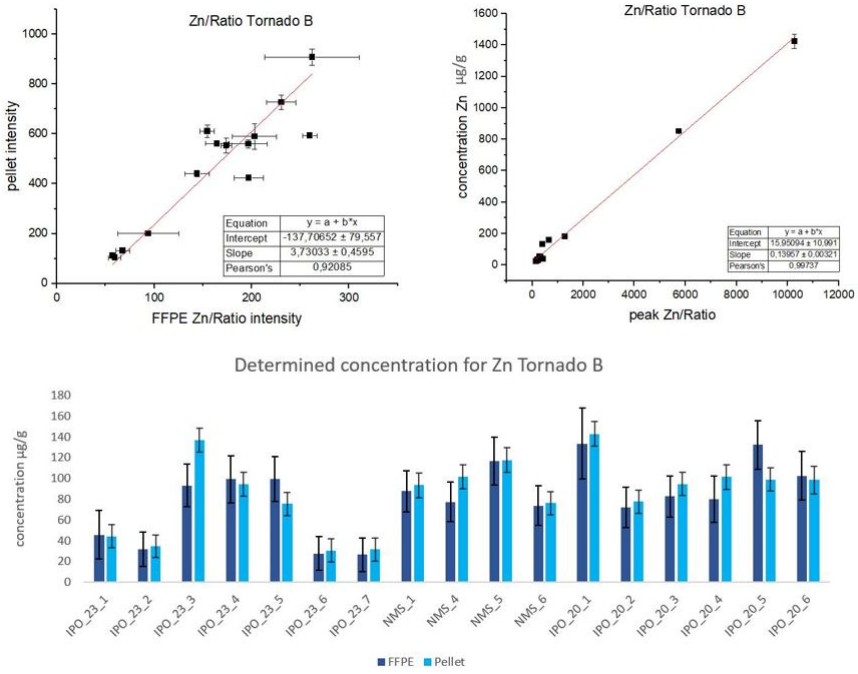

Figure 5.14: Analysis for Zn in configuration B. Up left: parametrization curve with Pearson's r = 0.921; up right: quantification curve with Pearson's r = 0.997. Bottom: plot of the calculated concentration for tissues in FFPE blocks and pellet.

5.3.2 Benchtop Results

Elemental calibration curves

To validate the curves constructed, the same procedure described before was adopted and in this case the CRM *GBW 07605 Tea* was used. The curves have been built by all of CRMs set for Fe, Cu and Zn, by 9 of them for Ca and by only 3 of them for Br. Having this reduced number of certified materials for Br made it not possible to withdraw one of the CRM from the set, thus the validation was performed using one of the three. The results of the validation (in μg/g) are shown in Table 5.5, along with the equation of the lines.

	CRM	Ref Value	Obtained value	% Δ	Equation
Ca	Tea	$(4.3\pm0.8)\cdot10^3$	$(4.8\pm0.6)\cdot10^3$	10.1	$y=(-4\pm5)\cdot10^2$ μg/g+$(22.2\pm0.9)\cdot x$
Fe	Tea	$(2.6\pm0.3)\cdot10^2$	$(3.1\pm0.3)\cdot10^2$	13.4	$y=(-40\pm20)$ μg/g+$(1.22\pm0.07)\cdot x$
Cu	Tea	17 ± 4	19 ± 4	10.1	$y=(-3\pm3)$ μg/g+$(0.37\pm0.02)\cdot x$
Zn	Tea	26 ± 4	24 ± 7	8.1	$y=(-19\pm6)$ μg/g+$(0.289\pm0.003)\cdot x$
Br	Tea	3 ± 1	3 ± 3	7.3	$y=(0.5\pm0.5)$ μg/g+$(0.085\pm0.009)\cdot x$

Table 5.5: Results of the validation of the quantification curves obtained for the benchtop triaxial system the CRM GBW 07605 Tea. Per each element the reference value, the obtained value and their percentage discrepancy (Δ) is reported. The equation of the quantification curves are shown in last column.

Tissue quantification

The parametrization of the formalin embedding effects on the dark matrix was performed between the normalized Kα peaks of the FFPE blocks and the respective tissues processed in pellets. A total of 5 elements were analyzed by this spectrometer, adding Br as a new element. To validate these curves IPO_23_3 has served as control sample. The obtained intensity compared with the measured ones and their percentage discrepancies are pictured in Figure 5.15. Following the same procedure adopted for Tornado, the intensities of the FFPE blocks had

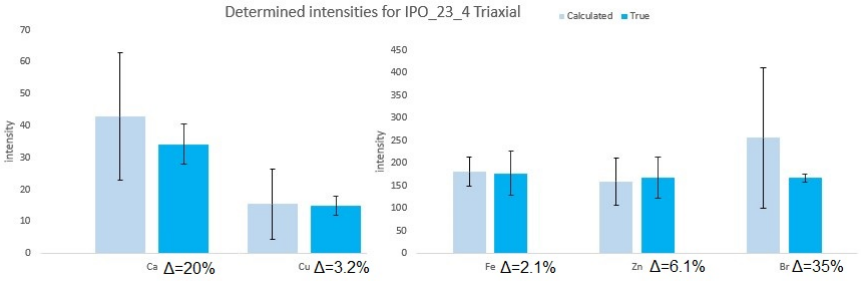

Figure 5.15: Plots of comparison between calculated and measured intensities and relative percentage discrepancies for the elements of interest of the sample IPO_23_4.

been transformed into *pellets intensities* and then quantified through the quantification curves obtained above. In this case the dataset was composed of NMS and IPO_23 samples only, due to the reasons explained in Chapter 4. The parametrization and quantification processes propagated the uncertainties, which are not negligible and in some cases lager than the calculated value itself. In Figures from 5.16 to 5.20 the two curves and the comparison per each sample of the concentration calculated for the tissues in pellets and in FFPE, for discrepancies smaller than 40%, are presented. The equation of the curves are summarized in Table 5.6

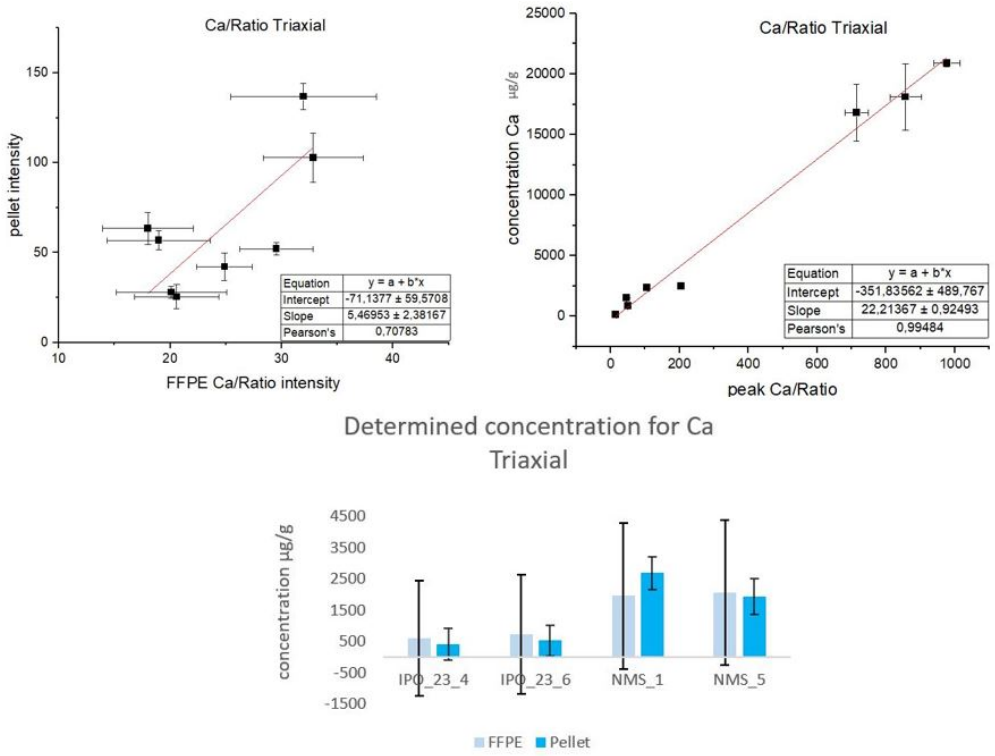

Figure 5.16: Analysis for Ca in the Triaxial benchtop spectrometer. Up left: parametrization curve with Pearson's r = 0.708; up right: quantification curve with Pearson's r = 0.995. Bottom: plot of the calculated concentration for tissues in FFPE blocks and pellet.

Element	Equation	Pearson's r
Ca	$y=(-7\pm6)\cdot10^{1}+(5\pm2)\cdot x$	0.708
Fe	$y=(1.2\pm0.2)\cdot10^{2}+(2.1\pm0.4)\cdot x$	0.878
Cu	$y=(-17\pm7)+(1.0\pm0.2)\cdot x$	0.921
Zn	$y=(5\pm4)\cdot10^{1}+(2.0\pm0.3)\cdot x$	0.932
Br	$y=(6\pm8)\cdot10^{1}+(15\pm5)\cdot x$	0.758

Table 5.6: Results of the parametrization curves obtained for the spectrometer Benchtop triaxial. Per each element the equation of the curve and the Pearson's r value are reported.

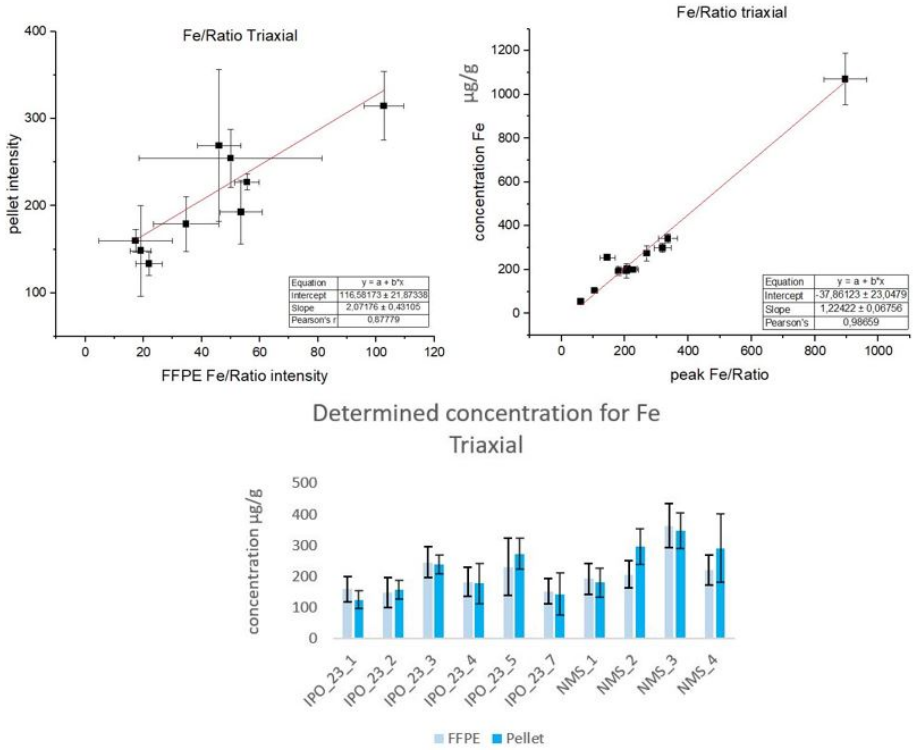

Figure 5.17: Analysis for Fe in the Triaxial benchtop spectrometer. Up left: parametrization curve with Pearson's r = 0.878; up right: quantification curve with Pearson's r = 0.987. Bottom: plot of the calculated concentration for tissues in FFPE blocks and pellet.

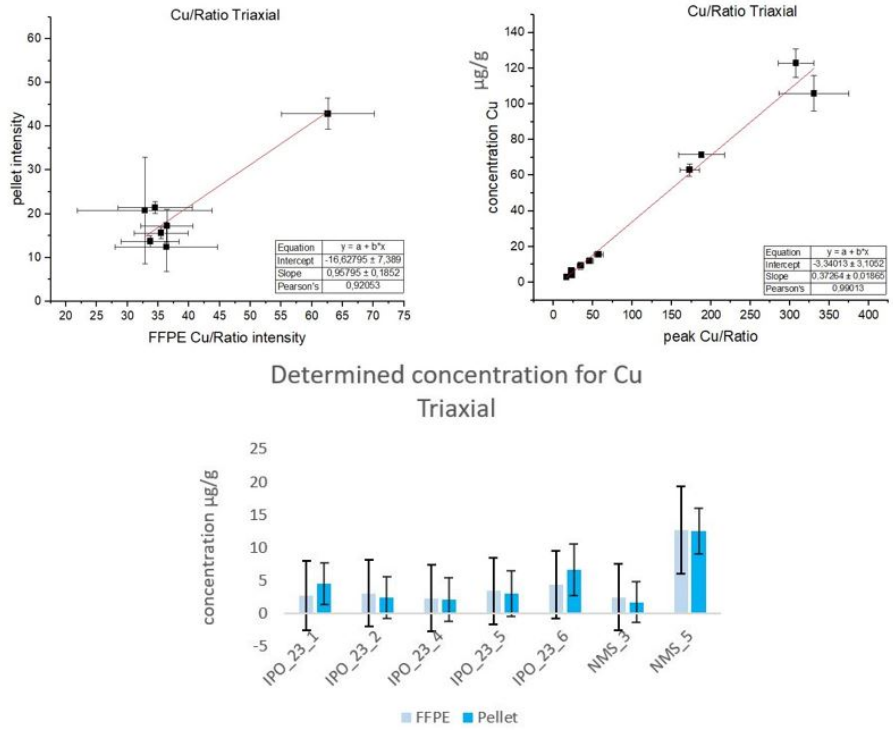

Figure 5.18: Analysis for Cu in the Triaxial benchtop spectrometer. Up left: parametrization curve with Pearson's r = 0.921; up right: quantification curve with Pearson's r = 0.990. Bottom: plot of the calculated concentration for tissues in FFPE blocks and pellet.

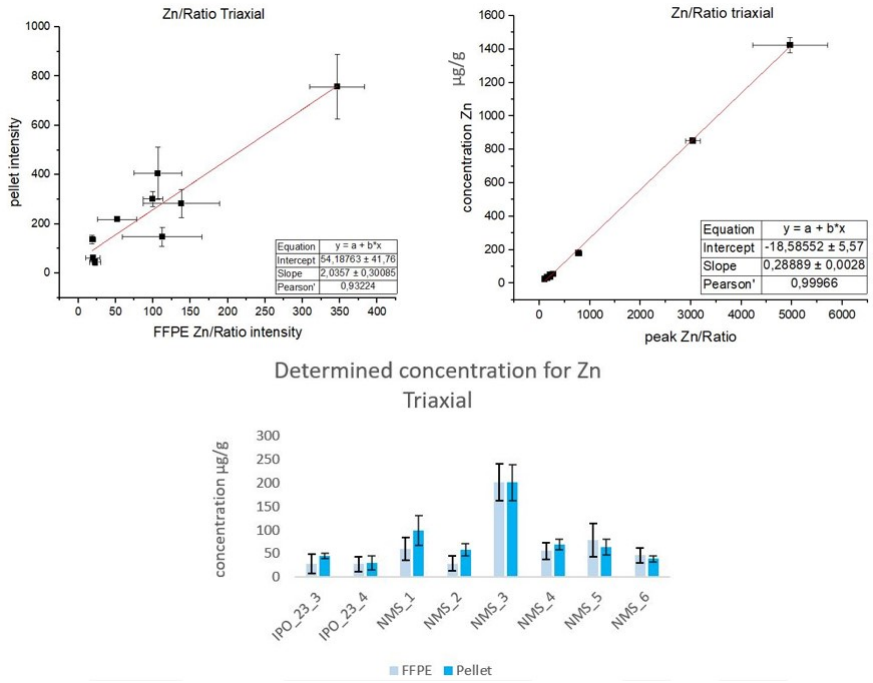

Figure 5.19: Analysis for Zn in the Triaxial benchtop spectrometer. Up left: parametrization curve with Pearson's r = 0.932; up right: quantification curve with Pearson's r = 0.999. Bottom: plot of the calculated concentration for tissues in FFPE blocks and pellet.

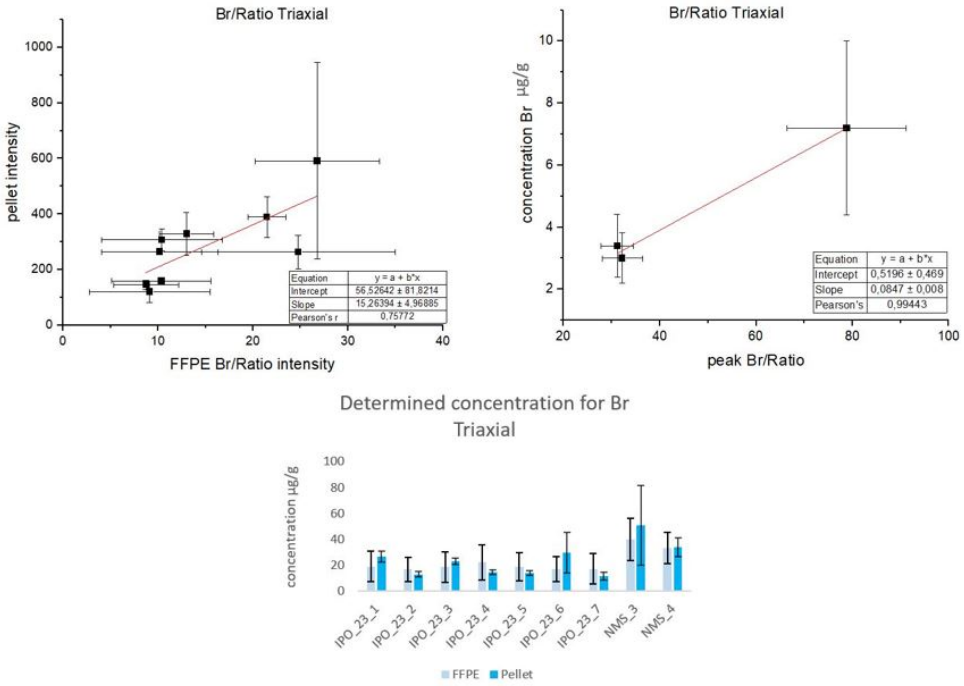

Figure 5.20: Analysis for Br in the Triaxial benchtop spectrometer. Up left: parametrization curve with Pearson's r = 0.758; up right: quantification curve with Pearson's r = 0.994. Bottom: plot of the calculated concentration for tissues in FFPE blocks and pellet.

5.4 Discussion

The use of three different systems and setups to analyze FFPE blocks allowed to study 7 elements from S to Br, and among the elements in common (Ca, Fe and Zn) to determine which one performs the most accurate quantification.

The Detection Limit of three setups differs, mostly due to their geometry, excitation energy and filters, as shown by the spectra of Figure 5.1. Furthermore, some elements were detected in tissues in pellet but not in FFPE blocks, which could be explained by the alteration of the matrix and absorption coefficient following the paraffin embedding process, or by the thickness of the tissue inside the FFPE block. This is the case, for instance, of FFPE block of the sample IPO_23_1 in the case of S, Ti and Cu. This indicates that its pellet inferred concentration of $(3.4\pm0.8)\cdot10^3\,\mu$g/g for S, $(40\pm50)\ \mu$g/g for Ti, and $(8\pm4)\mu$g/g for Cu were under the detection limit in the analysis of the blocks for Tornado. The results obtained per each element from the different analysis performed are summed up in the following paragraphs.

Sulfur-S

This element was detected in both FFPE and pellets only in Tornado, while in the Benchtop system it appeared only for some of the pellets, as the sample IPO_23_4. This could be due to the different exciting methods of the two spectrometers: Tornado excites using the Bremsstrahlung, while the Benchtop Triaxial system uses the energy of the secondary target (Mo) of 17.4 keV, reducing the photo-ionizing cross-section for S. By looking at the graphs and comparison of the concentrations obtained in Figure 5.6 and 5.10 only for 5 samples over the 17 analyzed presented discrepancies between the two values larger than 10% in configuration A, while configuration B shows poorer results, since more than half of the samples in the set present discrepancies larger than 20%. This results are compatible with higher Pearson's r values obtained for both of the curves for configuration A, than for the configuration that used a thicker filter along with higher mean-Z.

Calcium-Ca

This element, as Fe, was analyzed in all of the spectrometers, and its results are shown in the graphs and comparison of the concentrations obtained in Figure 5.7 and 5.11 for the two Tornado configurations, and in Figure 5.16 for the Benchtop spectrometer. For all of the three configurations the results are not very precise only for 6 samples in configuration A and 5 in configuration B, over the 19 analyzed, presented discrepancies between the two values lower than 35%. Regarding the concentration calculated for the Benchtop system only 3 out of 13 samples were below the 35% of discrepancy. This results are in line with the decreasing Pearson's r values obtained starting from Tornado in configuration A to the Benchtop.

Titanium-Ti

Due to its low characteristic energy, this element was detected only in Tornado with the thinnest filter of 12.5 μm of Aluminum, which allowed to filter out the background. However, only 4 of the set of CRMs had certified values for this element, which were also all quite low in concentration. This resulted in a poorer statistics of the quantification curve, that can be noticed in the large error bars of the concentration plot in Figure 5.8, and in the fact that only 4 samples out of 19 presented discrepancies between the pellets and FFPE quantified values lower than 45%.

Iron-Fe

Iron was detected by all of the spectrometers and with more accuracy than Ca. Results are shown in Figures 5.9, 5.12 and 5.17. Fe was the element with highest characteristic energy measured in Tornado with the thinnest filter. Even if the best Pearson's r value for the parametrization curve is the one obtained by Tornado in configuration B, the results of both of the configurations are not very accurate, having on a total of 19 samples analyzed, only 5 (A) and 7 (B) of them with discrepancies in the concentration of pellets and FFPE lower than 20%. Regarding the triaxial system, better results were obtained for the 13 samples, with discrepancies lower than 30% for 11 of them, and lower than 7% for 6 of them. There are three main differences in the spectrometers used: the geometry, the beam spot size and the excitation energy. For this element the triaxial geometry with secondary target of Molybdenum resulted in more accurate quantification of the concentration through the quantification curve. On the other hand, the larger spot size and the less precision in the positioning of the small area of interest of FFPE samples in front of the source had an impact in the study, resulting in a lower Pearson's r for the parametrization curve.

Copper-Cu

The analysis of this element were performed by Tornado in configuration B, where the filter of 100 μm of Al and 25 μm of Ti allowed it to emerge from the Bremsstrahlung radiation, and by the triaxial spectrometer, as can be seen in Figures 5.13 and 5.18. In this case the results of Tornado are more precise: of the 19 samples, only for 16 of them the element was detected in both FFPE and pellets, but for all of them the resulting discrepancies in the quantification is lower than 25%. The benchtop system didn't give such rigorous quantification and for 7 samples out of 13 the discrepancies were lower than 40%.

Zinc-Zn

Zn is the element with highest characteristic energy measured in Tornado between the two configurations. The curves represented in Figures 5.14 and 5.19 have similar Pearson's r, however more precise results are obtained from Tornado, where 15 out of 19 samples shown discrepancies in the concentration inferred for FFPE and pellets lower than 25%, while only 5 of 13 measured in the Benchtop reported the same discrepancy value.

Bromine-Br

Finally, Br is the highest characteristic energy element measured and quantified in FFPE blocks. Looking at Figure 5.20 it can easily be noticed that too few CRMs of the set used had this element certified, and because of this it was choosen to keep all of three CRMs in the quantification curve and not to exclude one for the validation. Despite of this, the results obtained for the quantification of the concentration in FFPE and pellets gave results compatible with the ones listed until now, with 6 pairs of samples with discrepancies lower than 30%.

Another consideration can be made on this element due to its energy. If the tissues stored in pellets are approximated for their attenuation coefficient and density by *ICRU-44 Soft Tissue* the thickness at which the sample can be considered infinite thick can be calculated. The infinite thickness value is obtained using the NIST data [35] in Formula 1.22 for the pellet mass attenuation coefficient of the incident radiation (Mo Kα), and of the element under study (Br Kα), recalling that in the triaxial geometry both the incident and the fluorescent angle measure

45°. A value of 5.9 mm is obtained as a threshold for the infinitely thick sample model. For most of the pellets analyzed this thickness was not reached, meaning that matrix effects are not negligible and sample dependent when studying Br. Only for Br this problem arises, since the pellets analyzed were thicker than the threshold of infinite thickness for the other elements studied in this system ($t_{Ca} = 0.3$ mm, $t_{Fe} = 1.3$ mm, $t_{Cu} = 2.6$ mm, and $t_{Zn} = 3.4$ mm).

Quantification curves slopes

Another aspect that deserve some attention is the attenuation of the characteristic radiation of the analyzed elements. By looking at the slopes of the quantification curves all of them decrease inversely with the characteristic energy of the element. Also, regarding the attenuation of the samples, it can be stated that the FFPEs peak intensities are smaller than the pellets' ones, as testified by the slopes of the parametrization curves, that are greater than 1 in all of the case, except for the parametrization curve of Cu for the triaxial system.

Conclusions

The main objective of this thesis was to parameterize the influence of paraffin embedding on the elemental study of human tissues, in order to be able to exploit the large amount of FFPE blocks collected and stored daily in hospital for trace elements quantification and their potential use as biomarkers for carcinogenesis.

During this work the main challenge has been given by tissues' quantity (19 paired samples suitable for Tornado and only 13 for the benchtop spectrometer) and their dimensions. The width of the tissues embedded in the blocks hindered their study in the portable spectrometer and made it not trivial for the benchtop system. Probably also their thickness played a role. The discrepancies found among the inferred mean-Z between the triaxial systems, which used different monochromatic excitation energies (Ge, Y and Mo), could be explained by too thin samples inside the blocks, resulting in signal from the paraffin behind when using higher energy beam, as for Molybdenum.

For what concerns the different spectrometers used, the triaxial system allows to remove the Bremsstrahlung radiation, making it possible to get signal form elements as Br, but the beam spot and intensity of the impinging radiation limit its application.

On the other hand, Tornado lets measure down to a spot size of 25 μm, get signal from lighter elements as S and present a more brilliant radiation source, but filters need to be applied in order to be able to get peaks emerging from the Bremsstrahlung.

Overall, the obtained FFPE parametrized intensities presented bias toward the values of their paired pellets lower than 9% for 11 of the total 13 parametrization curves built among the spectrometers, showing the potential of using EDXRF for the analysis of FFPE samples and applying conventional methods for quantification. However, the error propagation in this quantification process, due to the large uncertainties of the parameters of the built curves, results, in some cases, in uncertainties larger than the calculated value, indicating that improvements are needed. A larger paired set of samples, similar morphologically and of bigger dimensions could improve the research in this field and the results obtained both from the benchtop system and from the μ-EDXRF Tornado spectrometer, without having to deal with possible variation of the tissues thickness inside the FFPE blocks or issues in pellet preparation.

Bibliography

[1] WHO. *Detail of cancer*. Accessed on 31-07-2023. URL: https://www.who.int/news-room/fact-sheets/detail/cancer.

[2] Ana Ensina et al. "Analysis of human tissues using Energy Dispersive X Ray Fluorescence – Dark matrix determination for the application to cancer research". In: *Journal of Trace Elements in Medicine and Biology* 68 (2021), p. 126837. ISSN: 0946-672X. DOI: https://doi.org/10.1016/j.jtemb.2021.126837. URL: https://www.sciencedirect.com/science/article/pii/S0946672X21001279.

[3] Joanna Chwiej et al. "Preparation of tissue samples for X-ray fluorescence microscopy". In: *Spectrochimica Acta Part B: Atomic Spectroscopy* 60.12 (2005), pp. 1531–1537. ISSN: 0584-8547. DOI: https://doi.org/10.1016/j.sab.2005.10.002. URL: https://www.sciencedirect.com/science/article/pii/S0584854705002831.

[4] Sebastien C. Carpentier et al. "Lyophilization, a Practical Way to Store and Transport Tissues Prior to Protein Extraction for 2DE Analysis?" In: *Practical Proteomics* (2007). DOI: 10.1002/pmic.200700529.

[5] NOAA. *Electromagnetic Waves*. Accessed on 02-08-2023. URL: https://www.noaa.gov/jetstream/satellites/electromagnetic-waves.

[6] R. Van Grieken, A. Markowicz. *Handbook of X-ray Spectrometry*. CRC press, 2001.

[7] M. Haschke. *Laboratory micro-X-ray fluorescence spectroscopy*. Springer International Publishing, 2014.

[8] P. Brouwer. *Theory of XRF*. Almelo, Netherlands: PANalytical BV, 2006.

[9] Hubbell J. H.; Veigele Wm. J.; Briggs E. A.; Brown R. T.; Cromer D. T.; Howerton R. J. "Atomic form factors, incoherent scattering functions, and photon scattering cross sections". In: *Journal of Physical and Chemical Reference Data 1975-jul vol. 4 iss. 3* 4 (3 July 1975). DOI: 10.1063/1.555523. URL: libgen.li/file.php?md5=ef63cf08cf65b49da31b59d52571010c.

[10] Edmund Optics. Accessed on 07-08-2023. URL: https://www.edmundoptics.com/knowledge-center/application-notes/optics/introduction-to-polarization/.

[11] M. Guerra et al. "Theoretical and experimental study on the angular dependence of scattering processes in X-ray fluorescence systems". eng. In: *X-ray spectrometry* 42.5 (2013), pp. 402–407. ISSN: 0049-8246.

[12] H.G.J. Moseley M.A. "XCIII. The high-frequency spectra of the elements". In: *The London, Edinburgh, and Dublin Philosophical Magazine and Journal of Science* 26.156 (1913), pp. 1024–1034. DOI: 10.1080/14786441308635052. URL: https://doi.org/10.1080/14786441308635052.

[13] WALTER BAMBYNEK et al. "X-Ray Fluorescence Yields, Auger, and Coster-Kronig Transition Probabilities". In: *Rev. Mod. Phys.* 44 (4 1972), pp. 716–813. DOI: 10.1103/RevModPhys.44.716. URL: https://link.aps.org/doi/10.1103/RevModPhys.44.716.

[14] S. Pessanha et al. "A novel portable energy dispersive X-ray fluorescence spectrometer with triaxial geometry". In: *Journal of Instrumentation* 12.01 (Jan. 2017), P01014. DOI: 10.1088/1748-0221/12/01/P01014. URL: https://dx.doi.org/10.1088/1748-0221/12/01/P01014.

[15] ThermoFisher Scientific. Accessed on 05-08-2023. URL: https://www.thermofisher.com/blog/mining/technology-focus-silicon-drift-detectors/.

[16] Sofia Pessanha et al. "Detection limits evaluation of a portable energy dispersive X-ray fluorescence setup using different filter combinations: Evaluation of detection limits in EDXRF setup using different filters". eng. In: *X-ray spectrometry* 46.2 (2017), pp. 102–106. ISSN: 0049-8246.

[17] Rafał Sitko, Beata Zawisza. "Quantification in X-Ray Fluorescence Spectrometry". In: *X-Ray Spectroscopy*. Ed. by Shatendra K. Sharma. Rijeka: IntechOpen, 2012. Chap. 8. DOI: 10.5772/29367. URL: https://doi.org/10.5772/29367.

[18] Rafał Sitko. "Quantitative X-ray fluorescence analysis of samples of less than 'infinite thickness': Difficulties and possibilities". In: *Spectrochimica Acta Part B: Atomic Spectroscopy* 64.11 (2009), pp. 1161–1172. ISSN: 0584-8547. DOI: https://doi.org/10.1016/j.sab.2009.09.005. URL: https://www.sciencedirect.com/science/article/pii/S0584854709003176.

[19] T. Magalhães et al. "Trace elements in human cancerous and healthy tissues from the same individual: A comparative study by TXRF and EDXRF". In: *Spectrochimica Acta Part B: Atomic Spectroscopy* 61.10 (2006). TXRF-2005, 11th International Conference on Total Reflection X-ray Fluorescence Spectrometry and Related Methods, pp. 1185–1193. ISSN: 0584-8547. DOI: https://doi.org/10.1016/j.sab.2006.06.002. URL: https://www.sciencedirect.com/science/article/pii/S0584854706001716.

[20] T. Magalhães et al. "Study on trace elements behaviour in cancerous and healthy tissues of colon, breast and stomach: Total reflection X-ray fluorescence applications". eng. In: *Spectrochimica acta. Part B: Atomic spectroscopy* 65.6 (2010), pp. 493–498. ISSN: 0584-8547.

[21] Ana Ensina et al. "Analysis of human tissues using Energy Dispersive X Ray Fluorescence – Dark matrix determination for the application to cancer research". eng. In: *Journal of trace elements in medicine and biology* 68 (2021), pp. 126837–126837. ISSN: 0946-672X.

[22] Jorge Machado et al. "Accuracy improvement in XRF analysis for the quantification of elements ranging from tenths to thousands $\mu g\ g^{-1}$ in human tissues using different matrix reference materials". eng. In: *Journal of analytical atomic spectrometry* 35.12 (2020), pp. 2920–2927. ISSN: 0267-9477.

[23] I. Antcheva et al. "ROOT — A C++ framework for petabyte data storage, statistical analysis and visualization". eng. In: *Computer physics communications* 180.12 (2015), pp. 2499–2512. ISSN: 0010-4655. URL: http://root.cern.ch..

[24] Patrícia M.S. Carvalho et al. "Energy dispersive X-ray fluorescence quantitative analysis of biological samples with the external standard method". eng. In: *Spectrochimica acta. Part B: Atomic spectroscopy* 174 (2020), p. 105991. ISSN: 0584-8547.

[25] B.; Birschwilks M.; Vogt S.; Finney L.; Woloschak G. E. Paunesku T.; Wanzer M. B.; Kirillova E. N.; Muksinova K. N.; Revina V. S.; Lyubchansky E. R.; Grosche. "X-Ray Fluorescence Microscopy for Investigation of Archival Tissues". In: *Health Physics 2012-aug vol. 103 iss. 2* 103 (2 Aug. 2012). DOI: 10.1097/hp.0b013e31824e7023.

[26] Sofia Pessanha et al. "Evaluation of the influence of the formalin fixation time on the elemental content of tissues measured with X-ray fluorescence". In: *Spectrochimica Acta Part B: Atomic Spectroscopy* 205 (2023), p. 106704. ISSN: 0584-8547. DOI: https://doi.org/10.1016/j.sab.2023.106704. URL: https://www.sciencedirect.com/science/article/pii/S0584854723000915.

[27] Paweł M. Wróbel et al. "Feasibility study of elemental analysis of large population of formalin fixed paraffin embedded tissue samples – preliminary results". In: *Spectrochimica Acta Part B: Atomic Spectroscopy* 173 (2020), p. 105971. ISSN: 0584-8547. DOI: https://doi.org/10.1016/j.sab.2020.105971. URL: https://www.sciencedirect.com/science/article/pii/S0584854720304109.

[28] Sofia Pessanha et al. "A non-destructive X-ray fluorescence method of analysis of formalin fixed-paraffin embedded biopsied samples for biomarkers for breast and colon cancer". eng. In: *Talanta (Oxford)* 260 (2023), pp. 124605–124605. ISSN: 0039-9140.

[29] Bruker. *M4 Tornado*. Accessed on 05-08-2023. URL: https://www.bruker.%20com/en/products-and-solutions/elemental-analyzers/micro-xrf-spectrometers/%20m4-tornado.html.

[30] Pedro Amaro et al. "Validation of the Geant4 Monte Carlo package for X-ray fluorescence spectroscopy in triaxial geometry". eng. In: *Spectrochimica acta. Part B: Atomic spectroscopy* 130 (2017), pp. 60–66. ISSN: 0584-8547.

[31] Bright Spec. Accessed on 11-08-2023. URL: https://www.brightspec.be/brightspec/?q=node/31.

[32] Bright Spec. *bAxil User's manual*. version 2016.

[33] Yating Shen et al. "Matrix correction with Compton to Rayleigh ratio in a plant–soil–rock interface analysis using a laboratory micro-XRF". In: *X-ray spectrometry* (2019).

[34] Vasile-Dan Hodoroaba, Vanessa Rackwitz. "Gaining Improved Chemical Composition by Exploitation of Compton-to-Rayleigh Intensity Ratio in XRF Analysis". In: *Analytical Chemistry* 86.14 (2014). PMID: 24950635, pp. 6858–6864. DOI: 10.1021/ac5000619. eprint: https://doi.org/10.1021/ac5000619. URL: https://doi.org/10.1021/ac5000619.

[35] NIST. *Tissue, Soft (ICRU-44)*. visited 05-09-2023. URL: https://physics.nist.gov/PhysRefData/XrayMassCoef/ComTab/tissue.html.